Nano Research
2023, 16(5): 7119–7133

ISSN 1998-0124 CN 11-5974/O4
https://doi.org/10.1007/s12274-022-5302-6

Research Article

Quantitative tracking of trans-synaptic nose-to-brain transport of nanoparticles and its modulation by odor, aging, and Parkinson's disease

Alexander V. Romashchenko[1,2,8] (✉), Dmitrii V. Petrovskii[1], Sergey Yu. Trotsky[3], Ksenia N. Morozova[1], Nina B. Illarionova[1], Maria V. Zhukova[6], Elena V. Kiseleva[1], Marina B. Sharapova[1], Daniil S. Zuev[5], Konstantin E. Kuper[4], Sergey Yu. Taskaev[3,4], Anna I. Kasatova[3,4], Dmitrii A. Kasatov[3,4], Olga I. Solovieva[1], Ivan A. Razumov[1], Ludmila A. Gerlinskaya[1], Mikhail P. Moshkin[1], and Yuri M. Moshkin[1,7] (✉)

[1] *The Federal Research Center Institute of Cytology and Genetics, SB RAS, Academician Lavrentiev Avenue, 10, Novosibirsk 630090, Russia*
[2] *International tomography center, Institutskaya st., 3A, Novosibirsk 630090, Russia*
[3] *G. K. Boreskov Institute of Catalysis, SB RAS, Academician Lavrentiev Avenue, 5, Novosibirsk 630090, Russia*
[4] *The Federal Research Center Budker Institute of Nuclear Physics, SB RAS, Academician Lavrentiev Avenue, 11, Novosibirsk 630090, Russia*
[5] *Institute of Computational Technologies, Academician M.A. Lavrentiev avenue, 6, Novosibirsk 630090, Russia*
[6] *Institute of Gene Biology, Russian Academy of Sciences, Moscow 117334, Russia*
[7] *Institute of Molecular and Cellular Biology, SB RAS, Acad. Lavrentiev Ave, 8/2, Novosibirsk 630090, Russia*
[8] *Federal Research Centre of Biological Systems and Agrotechnologies, RAS, st. January 9, 29, Orenburg 460000, Russia*

Received: 7 August 2022 / **Revised:** 31 October 2022 / **Accepted:** 7 November 2022

ABSTRACT

Nanoparticles (NPs) can be transported via the nose-to-brain (N2B) route. Nonetheless, quantitative data on their spatiotemporal dynamics and regulation of the N2B transport are largely lacking. We surveyed metal oxide/hydroxide NPs as magnetic resonance imaging (MRI) contrasts for quantitative N2B tracking. NPs containing divalent transition metals were the only ones capable of N2B transmission. Using T_1-weighted (T_1W) MRI, we showed that Mn_3O_4-NPs were readily engulfed by olfactory receptor neurons (ORNs) without disrupting olfactory sensing, and we mapped their N2B trajectory. Within neurons, the Mn_3O_4-NPs were localized to the cytosol, mitochondria, and vesicles, and moved at mixed fast and slow axonal transport velocities intra- and extra-vesicularly through ORNs. The NPs' axonal transport is dependent on neuronal activity and microtubule integrity. The Mn_3O_4-NPs were trans-synaptically transmitted through at least four synapses across the olfactory tract. Trans-synaptic transmission of the NPs was dependent on N-type Ca^{2+} channels and NMDA receptors but blocked by $GABA_B$ receptor activation. A five-parameter Weibull signal increase/decrease model fitted to the T_1W MRI data allowed for estimating kinetic parameters of Mn_3O_4-NP accumulation/elimination. Absolute and relative accumulation rates, but not elimination, correlated negatively with the number of synapses from ORNs, indicating a coupling of the NPs' N2B transport with spontaneous neuronal activity. Accordingly, olfactory stimuli (2,5-dimethylpyrazine and acetophenone) significantly modulated and rerouted the Mn_3O_4-NP N2B transport odor specifically. Finally, the NPs' trans-synaptic transmission was impaired by aging and the onset of Parkinson's disease. These data suggest new approaches to diagnostics, functional neuroimaging, and controlling N2B drug delivery.

KEYWORDS

Mn_3O_4 nanoparticles, magnetic resonance imaging (MRI), nose-to-brain transport, trans-synaptic transmission, olfactory stimulation

1 Introduction

Certain viruses and nanoparticles (NPs) can be transmitted from the nasal cavity into the brain, thereby bypassing the blood-brain barrier. On the one hand, this property raises concerns over air-dispersed NPs as a risk factor for neurodegenerative diseases [1, 2]. On the other hand, this ability makes NPs attractive for the development of nose-to-brain (N2B) drug delivery systems, contrast dyes for neuroimaging, and other applications [3–8]. Nevertheless, further advances in these applications require precise quantification of NPs' N2B spatiotemporal dynamics and an understanding of mechanisms regulating and routing the neuronal trafficking of NPs.

In vitro-cultured neurons can engulf NPs as large as ~ 200 nm, and motor proteins can translocate the NPs along axons [9]. The neuronal uptake and axonal transport of NPs are thought to depend on their composition, surface properties, and size. Negatively, but not neutrally or positively, charged inorganic NPs, represented by, for example, quantum dots or metal oxides, are attracted by membranes and synaptic clefts of excitable neurons;

Address correspondence to Alexander V. Romashchenko, yuter2006@yandex.ru; Yuri M. Moshkin, yury.moshkin@gmail.com

清華大学出版社 Tsinghua University Press Springer

therefore, such particles are suitable for neuronal uptake [10, 11]. The shape and size (at least up to 100 nm) seem to have little impact on the neuronal uptake of inorganic NPs [11]. However, in these experiments [10, 11], the surface of NPs was coated by organic polymers (@PEG-COOH, @PEG-OCH_3, @PEG-NH_2, etc.) to control charge, which makes the conclusions about neuronal uptake of inorganic NPs less strict. Furthermore, for the organic, polystyrene NPs, both negatively and positively charged particles could be engulfed by neurons [12]. Such discrepancies show that the exact determinants of the NPs' neuronal uptake by large remain uncertain. Many other parameters (e.g., morphology and rigidity) may affect NPs' cellular uptake [13]. Positively and neutrally charged NPs are translocated along axons at rates comparable with slow axonal transport, whereas negatively charged ones travel at velocities similar to fast axonal transport [9, 12]. Additionally, the axonal transport rate of NPs depends on neuronal integrity and activity [9].

In vivo, the N2B transmission of NPs may be mediated by either diffusion through the paracellular space or neuronal uptake followed by axonal transport within olfactory or trigeminal nerves [6–8]. The latter route is of considerable interest for neuroimaging, drug delivery, and other applications. Upon intranasal administration, specific NPs accumulate in structures of the olfactory system (e.g., olfactory bulbs and anterior olfactory nuclei), the frontal cortex, hippocampus, striatum, nuclei of the brain stem (including the trigeminal nerve), and the cerebellum [6, 8]. Due to the N2B transmission of some NPs, several systems for *in vivo* neuroimaging have been developed. For example, exosomes loaded with gold NPs allow for computed tomography neuroimaging [3], and $CoFe_2O_4$@$BaTiO_3$ magnetoelectric NPs labeled with a near-infrared fluorochrome enable both near-infrared neuroimaging and magnetic resonance imaging (MRI) [5]. Despite growing interest in the N2B delivery route of drugs by NPs, quantitative dynamics of NPs' transport along the olfactory tract, the mechanism of their trans-synaptic translocation, and neuronal determinants of their N2B path have been characterized only scarcely.

To address this issue, we first surveyed the N2B transmission for a series of metal oxide/hydroxide NPs. Out of all tested NPs, only the NPs containing divalent transition metals (Mn^{2+}, Fe^{2+}, Co^{2+}, and Pt^{2+}) were accumulated and translocated from the olfactory epithelium (OE) to the main olfactory bulb (MOB). Fe^{2+} and Co^{2+} cations blocked the accumulation of the Mn_3O_4-NPs in the OE, suggesting the divalent metal transporter 1 (DMT1) in the neuronal uptake of NPs. For further analysis, we have selected the negatively charged Mn_3O_4 nanoparticles. *In vivo*, the Mn_3O_4-NPs were effectively transmitted across the olfactory tract, had high longitudinal relaxivity r_1 in the MOB, and did not affect odor recognition. We quantified their N2B spatiotemporal accumulation/elimination dynamics by the T_1-weighted (T_1W) MRI for 28 days after a single intranasal administration. The NPs relocated from the cilia of the OE to the MOB via axons of olfactory receptor neurons (ORNs) at velocities consistent on average with fast axonal transport. However, a significant fraction of the NPs was also transported at slow rates. The OE-to-MOB axonal transport of the NPs was intra- and extra-vesicular, microtubule-dependent, and required an ORN action potential. From the MOB's glomerular layer (GL), the NPs trans-synaptically moved to the mitral cell layer (ML). The GL-to-ML trans-synaptic transmission of the NPs required presynaptic voltage-gated N-type Ca^{2+} channels and postsynaptic NMDA receptors but was inhibited by the activation of presynaptic $GABA_B$ receptors. As assessed across the olfactory tract, the absolute and relative accumulation rates of the NPs correlated negatively with a putative number of synaptic connections from ORNs. The elimination rates were markedly slower and independent of a brain structure's position in the olfactory tract. Overall, the spatiotemporal dynamics of the Mn_3O_4-NPs N2B transmission were similar to those of the $Pt(OH)_2$-NPs. Odor stimuli rerouted the N2B transport of the Mn_3O_4-NPs to new brain structures associated with the respective stimuli, suggesting that the spontaneous or odor-evoked neuronal activity determines the NPs' N2B path and dynamics. Finally, the efficiency of GL-to-ML trans-synaptic transmission of the Mn_3O_4-NPs declined with aging and was impaired in Parkinson's disease (PD) mouse model strain expressing mutant alpha-synuclein (alpha-Syn^{A53T}). These findings uncover new possibilities for functional neuroimaging, odor-stimulated modulation of drug delivery, and diagnostics of neurodegenerations and age-related neuronal decline.

2 Results and discussion

2.1 Selectivity of neuronal uptake of the metal oxide/hydroxide NPs

To investigate the N2B neuronal uptake and transport of metal oxide/hydroxide NPs, we surveyed a series of T_1 (T_1W) and T_2* (T_2*W) weighted contrast NPs, and electron-dense ($Pt(OH)_2$ and $Ru(OH)_3$) NPs with similar (surface charge and size) physicochemical properties (Table S1 in the Electronic Supplementary Material (ESM)). The NPs were applied intranasally (7 μL at a concentration of 10 mg/mL) to BALB/c male mice. The accumulation of NPs was evaluated in the OE and MOB by the T_1W and T_2*W MRI (Fig. 1(a) and Fig. S1(a) in the ESM), micro-X-ray fluorescent (micro-XRF) analysis (Fig. 1(b)), and transmission electron microscopy (TEM) (Fig. S2(a) in the ESM).

We have shown a significant accumulation of the NPs containing Mn^{2+}, Fe^{2+}, and Co^{2+} in the OE and MOB one and twenty-four hours after intranasal administration, respectively (Fig. 1(a)). The $Pt(OH)_2$-NPs were detected in the MOB twenty-four hours after the administration by micro-XRF and TEM analysis (Fig. 1(b) and Fig. S2(a) in the ESM). Accumulation of this type of metal oxide NPs in the MOB, but not in the OE, was highly sensitive to colchicine, a known axonal transport inhibitor (Fig. S1(b) in the ESM). This suggests the predominant role of intracellular transport in their penetration into the brain. The NPs containing metal ions only in the oxidation state +3 (Mn_2O_3, Gd_2O_3, and $Ru(OH)_3$) and $MgFe_2O_4$-NPs carrying Mg^{2+} and Fe^{3+} were absent from the OE and MOB (Fig. 1). Such selectivity suggests that non-transferrin divalent cation transport system might mediate the neuronal uptake of metal oxide/hydroxide NPs. This hypothesis is supported, for example, by the substrate profile of the DMT1, which transports divalent transition metal ions (Mn^{2+}, Fe^{2+}, Co^{2+}, and Pt^{2+}), but not alkaline earth metal ions (Mg^{2+} and Ca^{2+}) or trivalent ions (Mn^{3+}, Fe^{3+}, Gd^{3+}, and Ru^{3+}). Furthermore, the DMT1 localizes to the mucociliary complex of the OE and mediates the Mn^{2+} olfactory uptake. In our experiments, we used surface-unmodified NPs, making possible a direct recognition of divalent transition metals on their lattice by DMT1 [14].

2.2 Synthesis, properties, and neuronal uptake of the Mn_3O_4-NPs

For further tracing experiments, the Mn_3O_4-NPs were selected as positive MRI contrast with the highest value of r_1 relaxivity among the other tested particles penetrating into the OE and MOB (Tables S1 and S2 in the ESM). To that, the Mn_3O_4-NPs had no effect on animals' ability to detect odor, 96 h after their intranasal

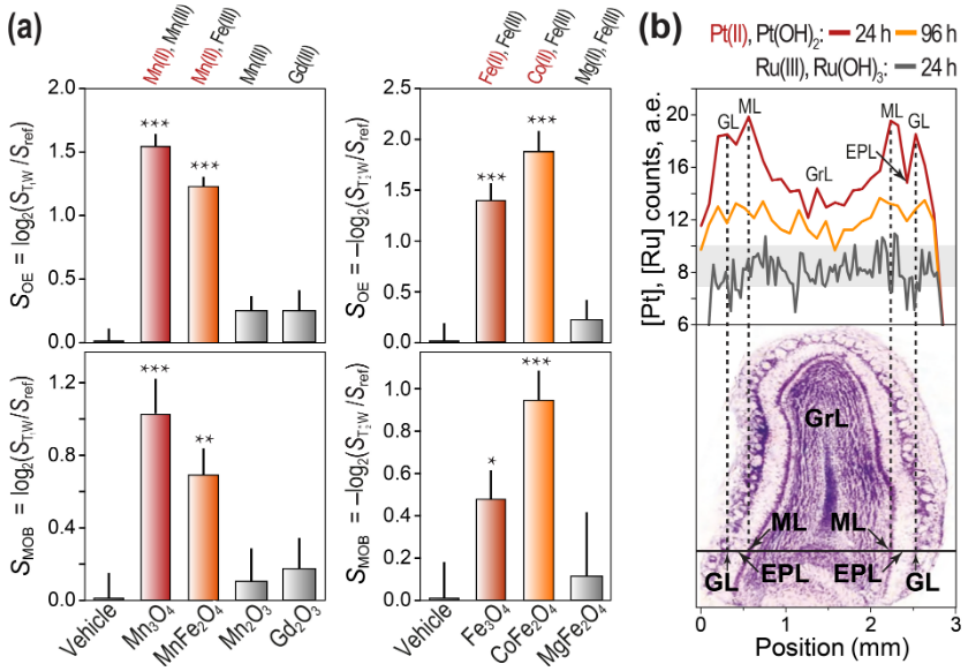

Figure 1 Selective uptake and N2B transmission of metal oxide/hydroxide nanoparticles. (a) The T_1-weighted (S_{T_1W}, left panel) and T_2*-weighted ($S_{T_2^*W}$, right panel) MRI signal intensities were assessed in the OE one hour after the intranasal administration of NPs (top panel) and in the MOB 24 h after the administration (bottom panel). The MRI signal intensities were normalized to that before the NPs' administration (S_{ref}) and compared to vehicle-treated animals (*$p < 0.05$, **$p < 0.01$, ***$p < 0.001$; *t*-test, $n = 6$ for each treatment). Bars denote the means and whiskers—standard errors of the mean (SEM). The oxidation states of the metals are indicated on the top. (b) The micro-XRF analysis of average [Pt] and [Ru] content (top panel) in fixed MOB slices (bottom panel). The [Pt] content was evaluated 24 (red curve) and 96 h (orange curve) after the intranasal administration of $Pt(OH)_2$-NPs, and the [Ru] content was measured 24 h after the administration of $Ru(OH)_3$-NPs (grey curve). The micro-XRF was performed on three biological replicates for each experiment. Note a significant increase in the [Pt] counts 24 h after the administration of $Pt(OH)_2$-NPs in the GL and ML of the MOB.

administration, suggesting that the Mn_3O_4-NPs do not interfere with the functional state of the olfactory system (Fig. S3(a) in the ESM). In human glioblastoma cells, the effects of the Mn_3O_4-NPs on cell viability were either nonsignificant or modest at concentrations of [Mn] exceeding physiological ~ 100 times, and compared to $MnCl_2$, the cytotoxicity of the Mn_3O_4-NPs was significantly lower (Fig. S3(b) in the ESM).

The Mn_3O_4-NPs were synthesized as previously described [15] with slight modifications (see the Methods section in the ESM). The core diameter of the synthesized NPs was ~ 34 nm, and their interplanar distances corresponded to Mn_3O_4 crystallites (Fig. S4(a) in the ESM). The hydrodynamic diameter (d_h) and zeta potential (ζ) of the Mn_3O_4-NPs were ~ 131.3 nm and approximately −18.1 mV, respectively (Fig. S4(b) in the ESM). r_1 at a magnetic field strength of 11.7 T varied from ~ 0.58 $mM^{-1}\cdot s^{-1}$ at neutral pH to > 1.28 $mM^{-1}\cdot s^{-1}$ in the presence of proteins and ~ 7.36 $mM^{-1}\cdot s^{-1}$ at pH 4.0 (Fig. S4(c) and Table S2 in the ESM). Notably, at acidic pH, the r_1 relaxivity of the Mn_3O_4-NPs was significantly higher than that of $MnCl_2$. The pH-dependency of r_1 has been reported previously for mesoporous MnO@mSiO$_2$ NPs [16]; likewise, the protein corona formed by intrinsically disordered proteins may also affect the r_1 [17, 18]. The Mn_3O_4-NPs were readily engulfed by *in vitro*-cultured mouse hippocampal neurons within 2 h of incubation and localized to the cytosol, autophagosomes, and synapses (the Methods section, and Figs. S4(d) and S4(e) in the ESM).

2.3 The N2B neuronal uptake of Mn_3O_4-NPs

To investigate the Mn_3O_4-NP neuronal uptake *in vivo*, we administered 7 μL of 10 mg/mL NPs into the right-side nostril of BALB/c male mice. Twenty-four hours after the administration, we evaluated the localization of the NPs in the OE and the GL of the MOB by TEM. The NPs were localized outside and inside the ORNs' cilia in the OE and transported to the dendritic knob (Fig. 2(a)). In the GL, the Mn_3O_4-NPs were detected in the cytosol and mitochondria of the ORN's axons (Fig. 2(a)). We also observed intra- and extra-vesicular localization of the NPs in axons and synapses of ORNs (Fig. 2(a)). We failed to detect Mn_3O_4-NPs by TEM in the contralateral bulb (left one), probably due to weak interbulbar connectivity (Fig. S5(a) in the ESM) [19]. These results suggest that ORN's cilium serves as a portal for the N2B transmission of NPs.

High-resolution TEM (HRTEM) measurements of interplanar distances of the engulfed NPs in the MOB combined with energy-dispersive X-ray microanalysis (EDXA) confirmed the presence of Mn_3O_4-NPs in the GL (Figs. S5(b) and S5(c) in the ESM). Inductively coupled plasma-atomic emission spectroscopy (ICP-AES) revealed that 0.58% ± 0.12% of the instilled Mn_3O_4-NPs accumulated in the MOB 24 h after the administration. The ICP-AES of MOB subcellular fractions showed significant enrichment of the NPs in mitochondrial and cytosolic fractions and lower accumulation in vesicular and nuclear fractions (Fig. 2(b)), which agrees with the TEM (Fig. 2(a)). The Mn_3O_4-NPs were absent from the extracellular space of the MOB (Fig. S5(d) in the ESM). Comparing Mn content by the ICP-AES in dialyzed and non-dialyzed cell lysates of the MOB obtained 24 h after the intranasal administration of either Mn_3O_4-NPs or $MnCl_2$ confirmed that the bulk of the Mn_3O_4-NPs accumulates in the MOB in a nanoparticulate form (Fig. S5(e) in the ESM).

The (in)solubility of Mn_3O_4-NPs was further investigated *in vitro* and in the U87 human glioblastoma cell line. In the U87 cells, the NPs were localized to endolysosomes after 2 and 48 h of incubation (Fig. S5(f) in the ESM). In the acidic environment of endolysosomes, the Mn_3O_4-NPs were partially dissolved as was

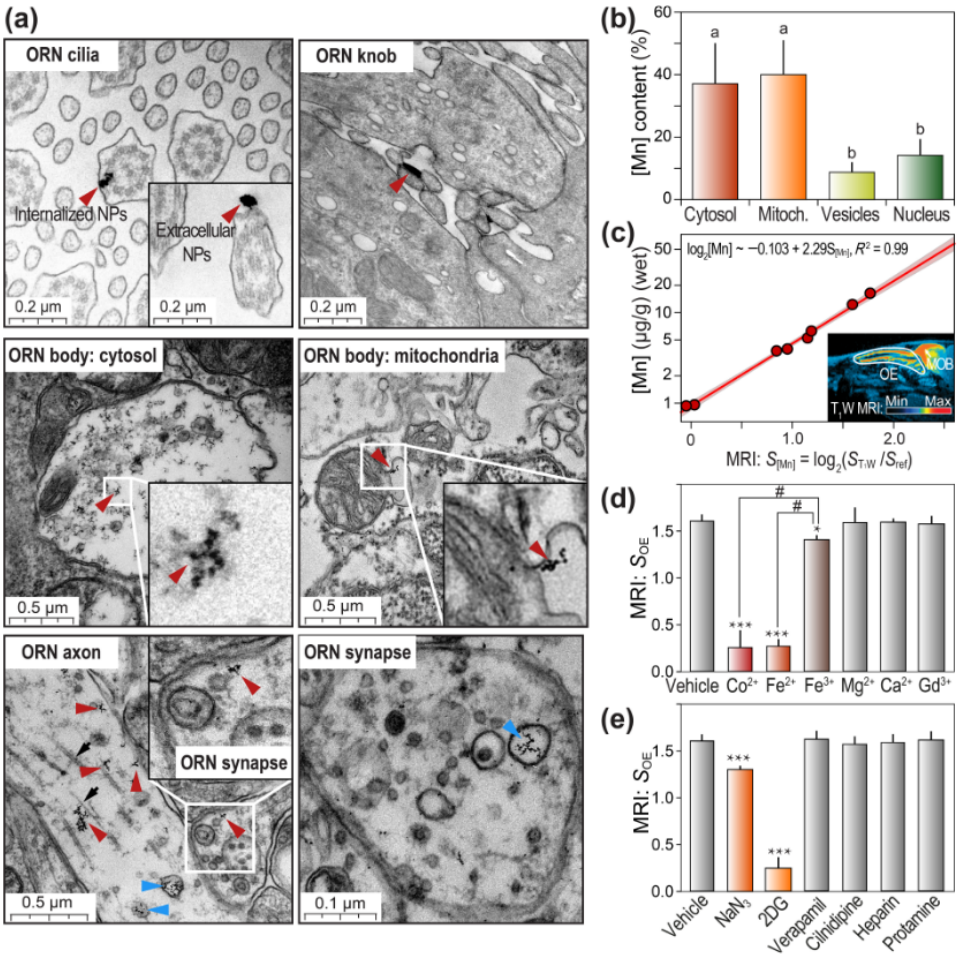

Figure 2 Neuronal uptake and subcellular localization of the intranasally administered Mn_3O_4-NPs in the OE and MOB. (a) TEM images of the cilia and bodies of ORNs in the OE and axons in the GL of MOB 24 h after the intranasal administration of Mn_3O_4-NPs (for control TEM, see Fig. S5(a) in the ESM). In the OE, the NPs were localized to ORNs' cilia (outside and inside) and knob (top panel). In the GL, the NPs were localized to cytosol and mitochondria of ORNs (middle panel). From ORN bodies, the Mn_3O_4-NPs were axonally transported to synapses (bottom panel) inside (blue arrows) and outside (red arrows) of the vesicles along the neuronal cytoskeleton (black arrows). The HRTEM-EDXA confirmed the presence of Mn_3O_4-NPs inside olfactory receptor neurons in the GL (Figs. S5(b) and S5(c) in the ESM). The interplanar distances of the engulfed NPs were 0.449 ± 0.036 nm (mean ± SEM), corresponding to the Mn_3O_4 crystallites (Fig. S5(b) in the ESM). (b) ICP-AES quantitation of the [Mn] content distribution among subcellular fractions of the MOB (% of the total [Mn] in the MOB) 24 h after the intranasal administration of Mn_3O_4-NPs. Bars denote the mean and whiskers—SEM; the letters indicate significant differences between groups (LSD test, $p \le 0.05$). (c) The relation between the concentrations of [Mn] in the MOB (μg per g wet tissue, as determined by ICP-AES) and normalized T_1W MRI signals, assessed 24 h after the intranasal administration of 7 μL of Mn_3O_4-NPs at various concentrations (0, 2, 4, or 6 mg/mL). The T_1W MRI signal intensities (S_{T_1W}) were normalized to the signal intensities at the same sites before the injection of NPs (S_{ref}) as $S_{[Mn]} = \log_2(S_{T_1W}/S_{ref})$. Inset, a representative pseudo-colored T_1W MRI image of the Mn_3O_4-NP accumulation in the OE and the MOB (sagittal plane). Effects of the intranasal pre-administration of (d) metal cations and (e) inhibitors of cell energy metabolism (NaN_3 and 2DG), blockers of L- and N/L-type Ca_v (verapamil and cilnidipine), polyanionic heparin and polycationic protamine (Table S3(a) in the ESM) on normalized T_1W MRI signal intensities quantified in the OE, one hour after the administration of Mn_3O_4-NPs. The T_1W MRI signal intensities were compared to vehicle-treated animals (*$p < 0.05$, ***$p < 0.001$; *t*-test, $n = 6$ for each treatment), and also between pre-administration of Fe^{3+}, Co^{2+}, and Fe^{2+} (#$p < 0.001$).

evidenced by a decrease in the size of NPs: from 38 ± 0.44 nm after 2 h of incubation to 28 ± 1.06 nm after 48 h of incubation (Fig. S5(g) in the ESM). Incubation of the NPs *in vitro* for 10 days showed that the Mn_3O_4-NPs were stable at pH 6.8. At pH 4.0, 11.89% ± 0.37% of Mn^{2+} ions were liberated from the surface of NPs into the solution (Fig. S5(h) in the ESM). Thus, it can be suggested that the bulk of the Mn_3O_4-NPs is stable in the MOB neurons as ~ 90% of the NPs were localized to the cellular compartments with neutral pH (cytosol, mitochondria, and nucleus). The remaining fraction of the NPs, which was localized to vesicular compartments with acidic pH (endolysosomes), may dissolve slowly releasing free Mn^{2+} at the average rate of ~ 0.05% per hour.

Next, we administered varying concentrations of the Mn_3O_4-NPs into the right-side nostril. Twenty-four hours later, we evaluated the Mn content of the MOB by ICP-AES and T_1W MRI. The T_1W MRI signal was normalized to the background (reference) signal obtained before the NPs administration to account for the endogenous [Mn] (Fig. 2(c) and Eq. (1) in Section 4). We noted a significant correlation between these two estimates for the Mn_3O_4-NPs. Both ICP-AES and T_1W MRI signals were increased following the administration of increasing doses of the Mn_3O_4-NPs (Fig. 2(c)). The ICP-AES estimate of the Mn content in the MOB of the control (mock-treated) animals was ~ 1 μg per g of wet tissue (or ~ 18.2 μM), which is in good agreement with physiological concentrations of [Mn] in the brain [20], substantiating the accuracy of ICP-AES measurements. After that, based on the ICP-AES evaluation of [Mn] content in the MOB, we estimated that *in vivo*, the r_1 relaxivity of Mn_3O_4-NPs was ~ 7.52 ± 0.67 $mM^{-1}·s^{-1}$ and of $MnCl_2$ ~ 5.02 ± 0.26 $mM^{-1}·s^{-1}$ (Table

S2 in the ESM). A statistically significant difference in the r_1 relaxivities of the nanoparticulate and soluble Mn in the MOB substantiates that, for the Mn_3O_4-NPs, the T_1W MRI signal corresponds to NPs but not to free Mn^{2+} ions. The enhanced *in vivo* r_1 relaxivity of the Mn_3O_4-NPs could be caused by the acidic environment of lysosomes and/or protein corona (Table S2 in the ESM). Given that the bulk of the NPs was localized outside of the vesicles in the MOB (Figs. 2(a) and 2(b)), it is likely that this enhancement is due to the protein corona.

Finally, to substantiate the possible role of the divalent cation transport system in neuronal uptake of the NPs, we applied high-affinity substrates (1 mM Co^{2+} and Fe^{2+}) of the DMT1 intranasally 10 min before administering the Mn_3O_4-NPs. One hour after the administration of NPs, the T_1W MRI analysis revealed a significant reduction in the Mn_3O_4-NPs accumulation in the OE, suggesting a competitive inhibition of neuronal uptake by these cations (Fig. 2(d)). Pre-administration of low-affinity substrates (1 mM Mg^{2+}, Ca^{2+}, and Gd^{3+}) had no effect, and 1 mM Fe^{3+} had little impact on the Mn_3O_4-NPs accumulation in the OE (Fig. 2(d)). As the DMT1 is energy-dependent transporter (a component of the non-transferrin divalent cation transport system) [21], prior administration of inhibitors of oxidative phosphorylation (NaN_3) and glycolysis (2-deoxy-D-glucose) lowered the accumulation of Mn_3O_4-NPs significantly in the OE (Fig. 2(e) and Table S3(a) in the ESM). Thus, the DMT1 might be involved in an energy-dependent neuronal uptake of the Mn_3O_4-NPs by ORNs' cilia. For a more detailed verification of the role of DMT1 in the neuronal uptake of divalent transition metal NPs in the future, it will be worth using gene DMT1 knockdown/knockout mice.

To further exclude the role of voltage-dependent calcium channels (Ca_v) in the neuronal uptake of Mn_3O_4-NPs, we pre-administered intranasally selective L- and N/L-type Ca_v blockers—verapamil and cilnidipine, respectively (Table S3(a) in the ESM). The pre-inhibition of Ca_v did not affect the T_1W MRI signal intensity in the OE (Fig. 2(e)). The pre-administration of heparin and protamine excluded a possible role of polyanion/polycation interactions of the Mn_3O_4-NPs with a neuronal membrane in their uptake (Fig. 2(e) and Table S3(a) in the ESM). Thus, the Mn_3O_4-NPs were suitable for quantitative MRI analysis of the NPs' N2B transport within the olfactory tract *in vivo*.

2.4 The N2B axonal and synaptic transmission of Mn_3O_4-NPs

Intracellular localization of the Mn_3O_4-NPs after their intranasal administration to axons and synapses was suggestive of axonal transport of the NPs from the OE to MOB. To confirm this, one hour after the Mn_3O_4-NP administration, we co-administered intranasally colchicine (1 mg/mL), an inhibitor of microtubule polymerization and axonal transport [22], brefeldin A (0.01 mg/mL), an inhibitor of fast vesicular axonal transport [23], or lidocaine (5 mg/mL), an inhibitor of voltage-gated Na^+ channels (Na_v) and ORN action potential [24, 25] (Table S3(b) in the ESM). Twenty-four hours after the administration, T_1W MRI revealed a significant accumulation of the Mn_3O_4-NPs in the OE of the control and treated animals (Figs. 3(a) and 3(b)). By contrast, normalized T_1W MRI signal intensities diminished significantly in the MOB of treated animals compared to the control (Fig. 3(b), and Figs. S6(a) and S6(b) in the ESM). Thus, if administered one hour later, colchicine, brefeldin A, or lidocaine did not interfere with neuronal uptake of the NPs in the OE but blocked their axonal transport to the MOB. These results are consistent with studies, suggesting that neuronal integrity and activity modulate the axonal transport rate of NPs [9]. Notably, unlike Mn_3O_4-NPs, brefeldin A increased the accumulation of $MnCl_2$ in the MOB (Fig. S6(d) in the ESM), pointing to different mechanisms of axonal transport of nanoparticulate [Mn] and free Mn^{2+} ions.

ORN axon terminals end in the MOB GL, synaptically connecting to the dendrites of mitral and tufted cells, residing in the MOB ML [26]. The Mn_3O_4-NPs were localized to the GL and ML, indicating their trans-synaptic transmission (Fig. 3(a) and Fig. S6(a) in the ESM). To identify the mechanism of the Mn_3O_4-NP trans-synaptic transmission, we applied several inhibitors of pre- and postsynaptic activity intranasally one hour after the administration of NPs.

Presynaptic inhibitors baclofen and cilnidipine administered at 0.5 mg/mL (Table S3(b) in the ESM) did not affect the Mn_3O_4-NPs' accumulation in the OE, but we noted a marked reduction in the ML-to-GL ratio in the T_1W MRI signal compared to the control (Fig. 3(c) and Fig. S6(c) in the ESM). Such reduction indicates inhibition of trans-synaptic transmission of the NPs. Baclofen is an agonist of presynaptic $GABA_B$ receptors, thus acting as an inhibitor of presynaptic activity [27]. Cilnidipine blocks N/L-type Ca_v, and in ORNs, the N-type Ca_v ($Ca_v2.2$) is critical for a presynaptic neurotransmitter release [28, 29]. These observations suggested that the trans-synaptic transmission of the NPs was modulated positively by the activity of presynaptic N-type Ca^{2+} channels but negatively by the GABAergic interneurons connected to ORNs.

Postsynaptic inhibitors 4,5,6,7-tetrahydroisothiazolo-[5,4-c]pyridin-3-ol (THIP) (gaboxadol; applied at 0.5 mg/mL) and IEM-1460 (1 mg/mL) did not affect the ML-to-GL ratio of the T_1W MRI signal (Fig. 3(c)). THIP is an agonist of the $GABA_A$ receptors expressed in mitral and tufted cells [30, 31], and IEM-1460 is an inhibitor of postsynaptic α-amino-3-hydroxy-5-methylisoxazole-4-proprionic acid (AMPA) receptors [32, 33] (Table S3(b) in the ESM). Nevertheless, we cannot rule out that the intranasally administered THIP and IEM-1460 reached the MOB. At the same time, a postsynaptic inhibitor of NMDA receptors, MK-801 [34], applied at 1 mg/mL, moderately but significantly lowered the ML-to-GL ratio of the T_1W MRI signal (Fig. 3(c) and Table S3(b) in the ESM). Thus, despite some study limitations, these results implied that the trans-synaptic transmission of the Mn_3O_4-NPs required pre- and postsynaptic activity modulated by the GABAergic interneurons, N-type Ca^{2+} channels, and NMDA receptors (Fig. 3(d)).

2.5 Spatiotemporal tracking of the N2B transmission of Mn_3O_4-NPs

T_1W MRI revealed that within 24 h, the Mn_3O_4-NPs were transported from the MOB through the lateral olfactory tract (LOT) to the lateral entorhinal cortex (ENTl) and the piriform cortex/cortical amygdala (PIR/CoA) (Fig. 4(a)). According to the known neuronal projections from the MOB [26], this pattern of the Mn_3O_4-NP accumulation matches two possible initial routes of the N2B transmission (Fig. 4(b))

$$\mathrm{OE} \underset{\mathrm{ORN}}{\rightarrow} \mathrm{GL} \overset{[1]}{\rightarrow} \mathrm{ML} \overset{[2]}{\underset{\mathrm{LOT}}{\rightarrow}} \{\mathrm{ENTl}, \mathrm{PIR/CoA}\}$$

These routes require at least two trans-synaptic transmission events, as indicated by the numbers above the arrows.

At 96 h after the Mn_3O_4-NP administration, we detected a significant increase in the T_1W MRI signal in the medial entorhinal cortex (ENTm), the hippocampus (dentate gyrus (DG) and Cornu Ammonis area 3 (CA3)), and the lateral septum (LS) (Fig. 4(a)). By following neuronal connections from the entorhinal cortex [35–38], we can propose that the initial ENTl N2B route extends further (Fig. 4(b)) as

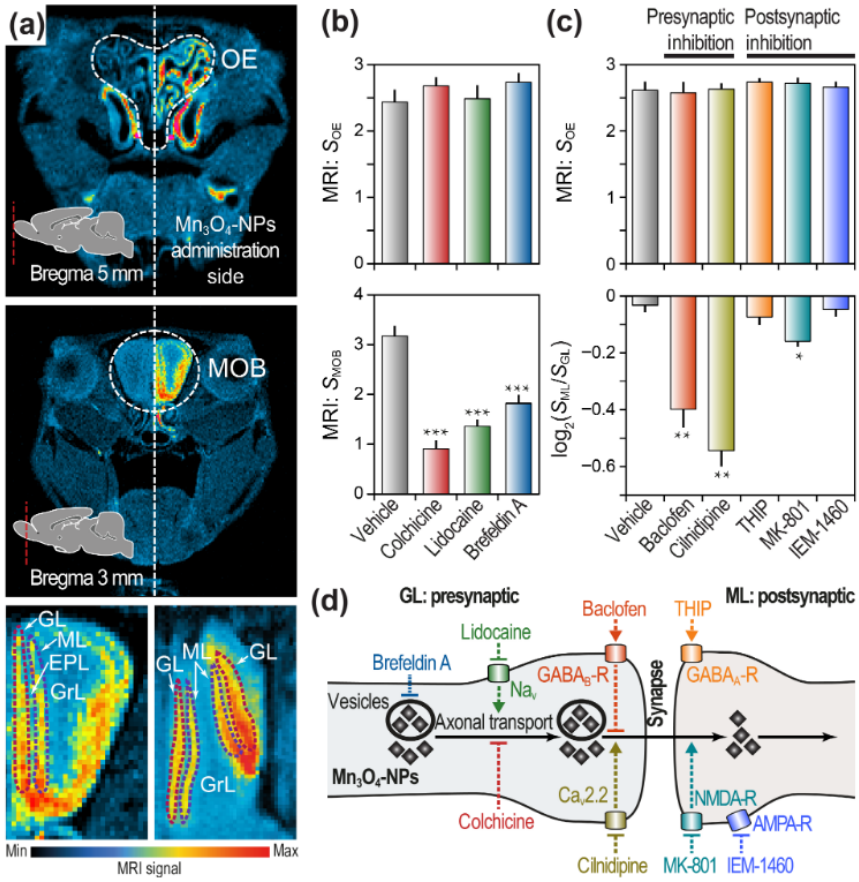

Figure 3 Axonal transport and trans-synaptic transmission of the Mn_3O_4-NPs. (a) T_1W MRI images of the OE (top panel) and MOB (middle panel) 24 h after the intranasal administration of Mn_3O_4-NPs into the right nostril (coronal plane). In the MOB (bottom panel), the Mn_3O_4-NPs localized to GL and ML (left—coronal, right—axial planes). The T_1W MRI signal intensities were significantly lower in the external plexiform (EPL) and granule cell (GrL) layers than in the GL and ML (Fig. S6(a) in the ESM). (b) Effects of colchicine, lidocaine, and brefeldin A on normalized T_1W MRI signal intensities quantified in the OE (top panel) and MOB (bottom panel) 24 h after the administration of Mn_3O_4-NPs. All significantly influenced the accumulation of Mn_3O_4-NPs in the MOB, but not in the OE, as compared to the control (***$p < 0.001$; *t*-test, $n = 6$ for each treatment) (Fig. S6(b) in the ESM). Bars indicate means and whiskers—SEM. (c) Effects of pre- and postsynaptic inhibition on the Mn_3O_4-NP transmission from the GL to ML 24 h after the administration of Mn_3O_4-NPs. Inhibitors of synaptic activity did not affect the T_1W MRI signal intensities in the OE (top panel). Bottom panel: inhibitors of presynaptic activity (baclofen and cilnidipine) and postsynaptic activity (MK-801) significantly reduced the ratio of T_1W MRI signal intensities between the ML and GL in comparison to the control (*$p < 0.05$, **$p < 0.01$; *t*-test, $n = 6$ for each treatment) (Fig. S6(c) in the ESM). Postsynaptic-activity inhibitors THIP (gaboxadol) and IEM-1460 had no effect. (d) A schematic diagram of the effects of the tested pharmaceuticals on the axonal transport and trans-synaptic transmission of the NPs (see the main text for details).

$$\text{ENTl} \xrightarrow{[3]} \text{ENTm} \xrightarrow{[4]} \text{DG}$$

$$\text{ENTl} \xrightarrow{[3]} \text{CA3} \xrightarrow{[4]} \text{LS}$$

In addition, we noted a significant accumulation of the NPs in the central amygdaloid nucleus (CeA) (Fig. 4(a)), which could be attributed to the neuronal projections from the CoA to CeA [39]. The CeA sends projections to the bed nucleus of the stria terminalis (BST), the substantia innominata of the ventral pallidum (SI), and the central nucleus of the inferior colliculus (IC) [26, 40, 41]. Consistent with this connectivity, 96 h after the Mn_3O_4-NP administration, the T_1W MRI signal increased in these regions, indicating additional routes of the Mn_3O_4-NPs' N2B transmission (Fig. 4(b))

$$\text{CoA} \xrightarrow{[3]} \text{CeA} \xrightarrow{[4]} \{\text{BST, SI, IC}\}$$

Thus, we conclude that the N2B transport of the Mn_3O_4-NPs requires multiple (at least four) trans-synaptic transmissions and proceeds along the following major olfactory routes

$$\text{OE} \underset{\text{ORN}}{\rightarrow} \text{GL} \xrightarrow{[1]} \text{ML} \underset{\text{LOT}}{\xrightarrow{[2]}} \{\text{ENTl, PIR/CoA}\} \xrightarrow{[3]} \{\text{ENTm, CA3, CeA}\} \xrightarrow{[4]} \{\text{DG, LS, BST, SI, IC}\}$$

A similar spatiotemporal distribution has also been observed for the $Pt(OH)_2$-NPs by the TEM and ICP-AES, indicating a common route for the NPs' N2B transmission. The $Pt(OH)_2$-NPs of a size less than 200 nm were accumulated in the MOB 24 h after the intranasal administration (Fig. 1(b), and Figs. S2(a) and S2(b) in the ESM). The size of the NPs transmitted to the MOB is likely limited by the diameter of olfactory receptor axons [42]. After 96 h, the $Pt(OH)_2$-NPs were eliminated from the MOB but accumulated in the PIR, CA3, and SI (Fig. 1(b), and Figs. S2(a) and S2(c) in the ESM).

2.6 Quantitative analysis of spatiotemporal dynamics of the Mn_3O_4-NPs' N2B transmission

Next, we quantitatively evaluated the spatiotemporal dynamics of the Mn_3O_4-NPs' N2B transport. To this end, for 28 days (672 h) after the administration, normalized T_1W MRI signal intensities (Eq. (1), see Section 4) were measured for six animals in each brain structure featuring significant accumulation of the Mn_3O_4-NPs (Figs. 4(a) and 4(b)). The accumulation phase of the Mn_3O_4-NPs was modeled using the Weibull cumulative distribution function (CDF) (Eq. (3), see Section 4) with two parameters:

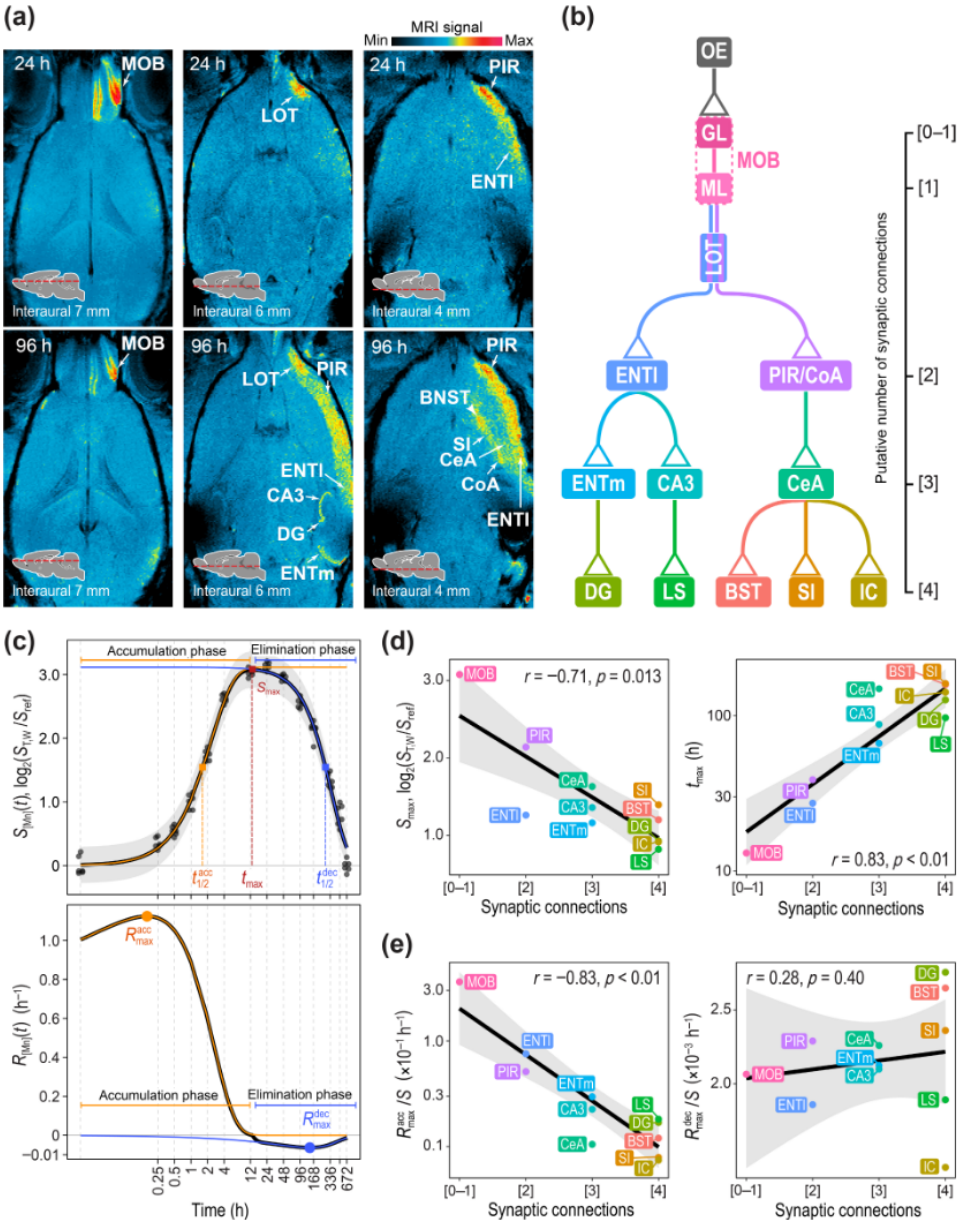

Figure 4 Quantitative dynamics of the N2B transport of the Mn_3O_4-NPs. (a) Distribution of the T_1W MRI signal on axial brain slices 24 and 96 h after the intranasal administration of Mn_3O_4-NPs into the right nostril. The brain structures with a significant increase in the normalized T_1W MRI signal are labeled. (b) The schematic diagram of the N2B transport of the Mn_3O_4-NPs along the olfactory tract based on known neuronal connections. Triangles represent synapses, and putative numbers of synaptic connections from the OE are indicated (see the main text for details). For the list of abbreviations, see Methods. (c) Top panel: The normalized T_1W MRI signal intensities ($S_{[Mn]}(t)$) were measured for six animals in the MOB across the indicated time points (dots). A five-parameter model (S_a, τ_{acc}, τ_{dec}, β_{acc}, and β_{dec}) was fitted to the $S_{[Mn]}(t)$ signal (black curve). The grey band corresponds to 95% confidence intervals of the prediction. The accumulation (orange) and elimination (blue) curves were plotted using the estimated parameters. The derived maximum of the T_1W MRI signal and time to it (S_{max} and t_{max}) as well as half-accumulation/elimination times ($t_{1/2}^{acc}$ and $t_{1/2}^{dec}$) are indicated. Note that S_{max} will always be slightly lower than asymptotic S_a. Bottom panel: The rates of the Mn_3O_4-NP accumulation/elimination ($R_{[Mn]}(t)$) were derived from the model. The accumulation phase corresponds to $R_{[Mn]}(t) > 0$ (orange curve), and elimination to $R_{[Mn]}(t) < 0$ (blue curve). The derived maximum accumulation/elimination rates (R_{max}^{acc} and R_{max}^{dec}) are presented. See also Fig. S7, Tables S4 and S5 in the ESM for the accumulation/elimination dynamics of the Mn_3O_4-NP along the olfactory tract. Spearman correlations of (d) S_{max} and t_{max}, and (e) relative maximum accumulation/elimination rates (R_{max}^{acc}/S_{max} and R_{max}^{dec}/S_{max}) with the putative number of synaptic connections from the OE (Table S5 in the ESM).

characteristic accumulation time τ_{acc} and shape β_{acc}. The elimination phase was modeled via the complement CDF (Eq. (4), see Section 4), where τ_{dec} and β_{dec} correspond to characteristic elimination time and shape, respectively. By combining $F_{acc}(t)$ and $F_{dec}(t)$, we modeled $S_{[Mn]}(t)$ for each brain structure as $S_{[Mn]}(t) = S_a F_{acc}(t) F_{dec}(t)$ (Eq. (2), see Section 4), where S_a corresponds to the asymptotic maximum of $S_{[Mn]}(t)$ (Fig. 4(c) and Fig. S7(a) in the ESM). Upon estimation of the models' parameters S_a, τ_{acc}, τ_{dec}, β_{acc}, and β_{dec} (Table S4 in the ESM), the rates of Mn_3O_4-NPs accumulation/elimination were derived as Eq. (5) (see Section 4, Fig. 4(c) and Fig. S7(b) in the ESM). As a result, kinetic parameters, such as accumulation/elimination times and rates, of the Mn_3O_4-NPs' N2B transport dynamics were derived (Table S5 in the ESM). We also used alternative CDFs to

model $S_{[Mn]}(t)$. The root-mean-square deviations were comparable between the models based on the Weibull and Gamma CDFs, and both are suitable for modeling arrival times. Other models (based on the Logistic and Gompertz CDFs) fitted the data poorly.

In this analysis, we first noticed that the mean accumulation time of Mn_3O_4-NPs in the MOB was ~ 2.31 h (Table S5 in the ESM). From this, it follows that, on average, axonal transport velocities for the Mn_3O_4-NPs are ~ 50–85 mm/day because the length of ORN axons is ~ 5–8 mm [6]. Such velocities are close to the vesicular and mitochondrial fast axonal transport (~ 100 mm/day) [43], substantiating the effects of brefeldin A (Fig. 3(b)) and intracellular localization of ~ 46% of the NPs to mitochondria and vesicles (Figs. 2(a) and 2(b)). Nonetheless, a significant proportion of the NPs moved at slower velocities of ~ 9–15 mm/day because t_{max} [time to maximum $S_{[Mn]}(t)$] for the MOB was ~ 13 h (Fig. 4(c) and Table S5 in the ESM). These speeds are comparable with slow-axonal-transport characteristic for cytosolic supramolecular complexes [43]. Approximately 40% of the Mn_3O_4-NPs localized to the cytosol (Figs. 2(a) and 2(b)), where they could associate with intrinsically disordered proteins [18] and be transported as a part of supramolecular complexes.

Second, estimated maxima (S_{max}) of the $S_{[Mn]}$, time to the half-accumulation ($t^{acc}_{1/2}$) and maximum accumulation (t_{max}), and maximum accumulation rates (R^{acc}_{max}) correlated negatively with the putative number of synaptic connections from the OE, substantiating our reconstruction of the N2B transport route for the Mn_3O_4-NPs (Fig. 4(d) and Fig. S8 in the ESM). The maxima of relative accumulation rates (R^{acc}_{max}/S_{max}) were also inversely proportional to the putative number of synaptic connections (Fig. 4(e)). These relations indicate the NPs' N2B transport coupling with the olfactory neuronal network activity. Indeed, the spontaneous neuronal activity of ORNs is coordinated throughout the olfactory tract [44–46], and the axonal transport and trans-synaptic transmission of the NPs are neuronal-activity dependent (Fig. 3).

Third, the elimination rates were markedly slower than the accumulation rates and did not correlate with the putative number of synaptic connections (Fig. 4(e) and Fig. S8 in the ESM), suggesting a passive clearance mechanism due to either exocytosis or slow dissolution of the Mn_3O_4-NPs.

Finally, because the normalized T_1W MRI signal correlated with the Mn content determined by ICP-AES (Fig. 2(c)), it was possible to recalibrate the Mn_3O_4-NP accumulation/elimination models and estimate maximum concentrations of Mn in individual brain structures (Table S5 in the ESM). In the MOB, the maximum accumulation of nanoparticulate [Mn] was ~ 123.66 μg per g of wet tissue (~ 2.25 mM), which exceeds physiological concentrations of [Mn] about 100 times [20]. Although such a concentration of nanoparticulate [Mn] was moderately cytotoxic for U87 cells, it did not impair olfactory recognition in mice (Fig. S3 in the ESM). Downstream of the MOB, the accumulation of nanoparticulate [Mn] dropped sharply to non-toxic for U87 cell concentrations (Fig. S3(b) and Table S5 in the ESM). Thus, the Mn_3O_4-NP could be a relatively safe probe for quantitative neuroimaging *in vivo*.

2.7 Odor-induced modulation of the N2B transmission of Mn_3O_4-NPs

Given that the N2B transport of Mn_3O_4-NPs depends on neuronal activity, we wondered whether olfactory stimuli could modulate it. To this end, between 24 and 48 h after the intranasal administration Mn_3O_4-NPs, we presented 2,5-dimethylpyrazine (2,5DMP) or acetophenone (PhAc) odor stimuli to mice in 10 sessions for 5 min with 55 min intervals using an olfactometer (Fig. S9 in the ESM). The T_1W MRIs were recorded and quantified for distinct brain structures 24 and 48 h after the NPs' administration. The T_1W signal intensities were expressed as $\log_2(S_{48h}/S_{24h})$ ratios, representing a change in $S_{[Mn]}$.

Exposure of the BALB/c male mice to 2,5DMP induced de novo accumulation of the Mn_3O_4-NPs in the perirhinal area (PERI), primary visual area (VISp), and primary somatosensory area (SSp) as compared to air-stimulated mice (Figs. 5(a) and 5(b)). In addition, we registered a significant decrease in T_1W signal intensities in the CoA and IC located along the N2B route

$$\text{MOB} \xrightarrow{[2]} \text{CoA} \xrightarrow{[3]} \text{CeA} \xrightarrow{[4]} \text{IC}$$

The PERI receives inputs from PIR and outputs axons to the interconnected VISp and SSp [47, 48], suggesting that 2,5DMP unlocks a new N2B transport route for the Mn_3O_4-NPs (Fig. 5(c))

$$\text{MOB} \xrightarrow{[2]} \text{PIR} \xrightarrow{[3]} \text{PERI} \xrightarrow{[4]} \{\text{VISp}, \text{SSp}\}$$

PhAc led to a significant de novo enhancement of the T_1W MRI signals in the anterior olfactory nuclei (AON), olfactory tubercles (OT), medial amygdalar nucleus (MEA), magnocellular nucleus (MA), agranular insular area (AI), substantia nigra (SNr), and subthalamic nucleus (STN) (Figs. 5(d)–5(f)). Besides, it increased T_1W MRI signals in the PIR, CeA, and CA3 located along the N2B routes

$$\text{MOB} \xrightarrow{[2]} \{\text{PIR}/\text{CoA}\} \xrightarrow{[3]} \text{CeA and MOB} \xrightarrow{[2]} \text{ENTl} \xrightarrow{[3]} \text{CA3}$$

The AON and OT are directly involved in processing olfactory information, and thus the NPs could be transmitted into these structures directly from the MOB ML [49]. The PhAc-stimulated N2B transport of the NPs to the MEA and MA could occur via the PIR [50, 51]. Finally, the NPs could be redirected from the CeA to the AI, SNr, and STN under the PhAc olfactory stimulation [52–54].

Thus, olfactory stimulation caused pronounced rerouting of the N2B transport of Mn_3O_4-NPs in an odor-specific manner. Olfactory modulation of the N2B transport has also been demonstrated for soluble Mn^{2+} in manganese-enhanced MRI studies [55]. Although it remains to be investigated how closely the N2B transport of NPs mirrors that of free Mn^{2+}, both systems could be used complementarily for functional MRI to evaluate distinct neuronal/synaptic activity parameters.

2.8 Effects of aging and Parkinson's disease on the N2B transmission of Mn_3O_4-NPs

Aging and neurodegenerative diseases are associated with olfactory dysfunction [56]. Thus, we wondered whether the N2B transmission of NPs is affected by aging and/or PD. To this end, we applied the Mn_3O_4-NPs intranasally to the C57BL/6 and hualpha-Syn(A53T) male mice aged 8, 30, and 38 weeks. The hualpha-Syn(A53T) is a transgenic mouse model strain of the PD, expressing the A53T mutant form of human alpha-synuclein (alpha-Syn^{A53T}) in the C57BL/6 background and developing olfactory dysfunction with age [57, 58]. The accumulation of the Mn_3O_4-NPs was quantitatively evaluated in the GL and ML layers of the MOB by the T_1W MRI.

We observed significant differences in the NPs' accumulation dynamics between C57BL/6 and hualpha-Syn(A53T) male mice aged 8 and 38 weeks (Fig. S10 in the ESM). The asymptotic maximum of the T_1W MRI signal was significantly higher in the GL of hualpha-Syn(A53T) compared to C57BL/6 male mice aged eight weeks (Table S6 in the ESM). However, in mice aged 38 weeks, the accumulation of NPs was significantly reduced in the GL and ML of hualpha-Syn(A53T) compared to C57BL/6 (Table S6 in the ESM).

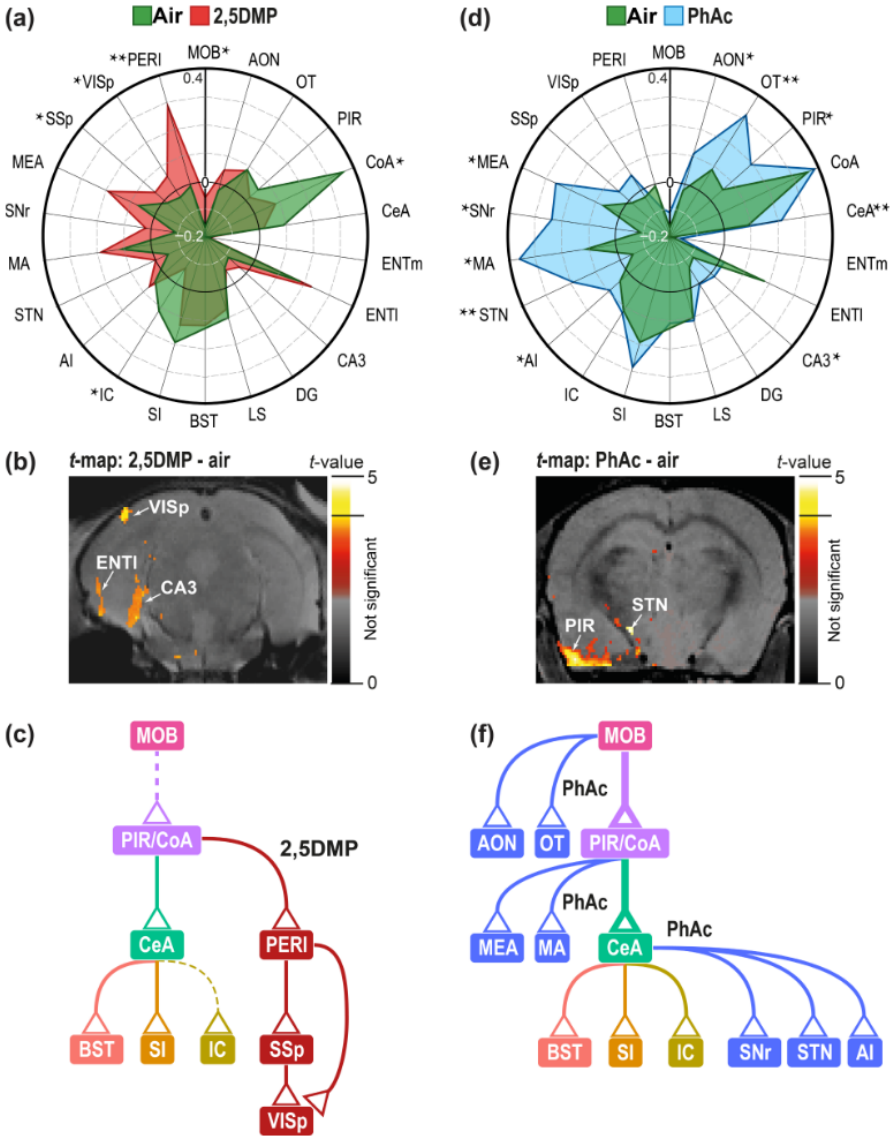

Figure 5 Olfactory stimulation modulates the trajectory of Mn_3O_4-NP N2B transport. (a) A radar chart of Mn_3O_4-NP distribution patterns in the brain of odor-stimulated (red area, 2,5DMP) and unstimulated (green area) animals. The odor was presented 24 h after the administration of NPs (ten times for 5 min during 10 h). $S_{[Mn]}$ was evaluated before and after the odor presentation (24 and 48 h after the administration of NPs) and expressed as $\log_2(S_{48h}/S_{24h})$. The $\log_2(S_{48h}/S_{24h})$ coordinate is depicted as a black vertical line, and coordinate circles are plotted with a step of 0.1. $^*p < 0.05$ and $^{**}p < 0.01$ significant differences in $\log_2(S_{48h}/S_{24h})$ between the odor-stimulated animals and the air-stimulated group (*t*-test). (b) The *t*-map (MRI map of the *t*-test values) of differences in $\log_2(S_{48h}/S_{24h})$ ratios between the 2,5DMP-stimulated and control animals. The color key and a significance cut-off for the *t* values are indicated (grey, red, and orange: nonsignificant, and yellow: significant). (c) A schematic diagram of deviations in the N2B transport of the Mn_3O_4-NPs along the olfactory tract upon the stimulation with 2,5DMP. New structures and synaptic connections between them are highlighted in red. Note that for the CoA and IC, the $\log_2(S_{48h}/S_{24h})$ ratio diminished after the exposure to 2,5DMP (indicated as dashed lines). (d) A radar chart, (e) *t*-map, and (f) a schematic diagram of the Mn_3O_4-NPs distribution patterns after the presentation of PhAc. Note that for the PIR and CeA, the $\log_2(S_{48h}/S_{24h})$ ratios increased after the presentation of PhAc and are indicated as thick lines. New structures and synaptic connections between them are highlighted in blue.

The trans-synaptic transmission of Mn_3O_4-NPs from the GL to ML was significantly impaired in hualpha-Syn(A53T) male mice compared to C57BL/6 at all ages (Fig. 6(a)). From the age of 30 weeks, the root-mean-square deviation from the reference (C57BL/6) model of trans-synaptic transmission dynamics confidently discriminated individuals expressing the mutant alpha-Syn^{A53T} from wild-type (Fig. 6(b)). Moreover, the model-fitted maxima of the ML-to-GL ratios declined with age in both C57BL/6 and hualpha-Syn(A53T) male mice, suggesting an age-related inhibition of the NPs' trans-synaptic transmission (Fig. 6(c)).

Thus, we concluded that age- and alpha-Syn^{A53T}-related reduction in the Mn_3O_4-NPs trans-synaptic transmission in the MOB might be correlated with olfactory dysfunction and neuronal decline.

3 Conclusions

N2B transport has attracted much attention regarding drug delivery, neuroimaging, and other applications involving nanoparticles as cargo, contrast agents, or both [4, 6–8, 59]. Nonetheless, the information about the mechanism of NPs' neuronal transport, trans-synaptic transmission, and quantitative parameters of the N2B transport is scarce.

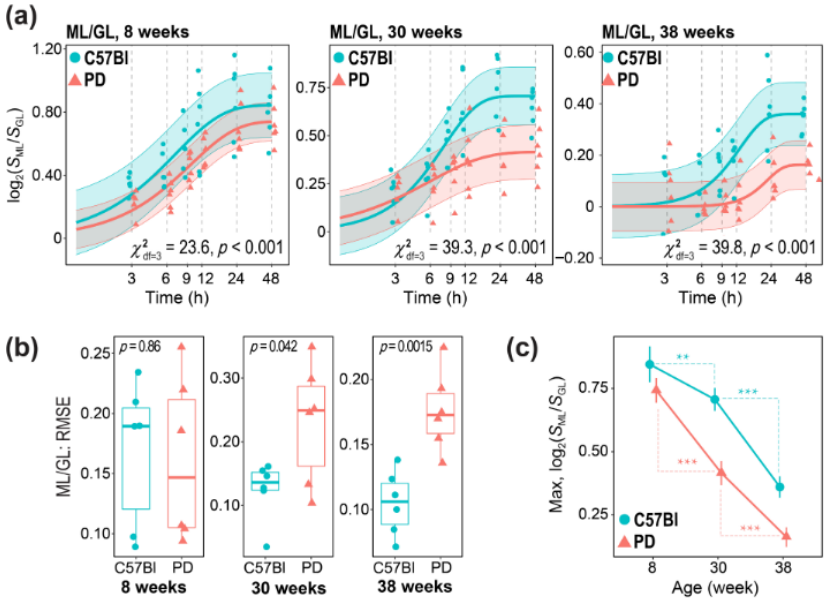

Figure 6 Aging and the onset of neurodegeneration impair the GL-to-ML trans-synaptic transmission of the Mn_3O_4-NPs. (a) The dynamics of Mn_3O_4-NPs trans-synaptic transmission were evaluated in C57BL/6 (green circles) and hualpha-Syn(A53T) (red triangles) male mice aged 8, 30, and 38 weeks (six animals for each experimental group). The hualpha-Syn(A53T) is a transgenic Parkinson's disease mouse model strain (PD). The trans-synaptic transmission was expressed as $\log_2$ of the ML-to-GL ratio of normalized T_1W MRI signals (Fig. S10 in the ESM). Three-parameter Weibull models were fitted for C57BL/6 (green line) and PD (red line) (Table S6 in the ESM), and the likelihood-ratio test was used to assess the effect of a strain on trans-synaptic transmission dynamics at each age. Filled ribbons represent 95% confidence intervals of the predictions. (b) RMSE deviation from the reference (C57BL/6) model of GL-to-ML trans-synaptic transmission dynamics estimated for the C57BL/6 and PD individual male mice identifies the onset of neurodegeneration in the PD mice from the age of 30 weeks. (c) The GL-to-ML trans-synaptic transmission of the Mn_3O_4-NPs declines with aging. The model estimated asymptotic maximums of the $\log_2(S_{ML}/S_{GL})$ decreased significantly with age for the C57BL/6 and hualpha-Syn(A53T) (PD) male mice (***$p < 0.001$).

A survey of metal oxide/hydroxide NPs revealed that only NPs accumulating in the OE and transported to the MOB were the ones that contained divalent transition metals (Mn^{2+}, Fe^{2+}, Co^{2+}, and Pt^{2+}). Accumulation of the Mn_3O_4-NPs in the OE was blocked by Co^{2+} and Fe^{2+}, suggesting a possible role of the non-transferrin divalent cation transport system, represented by the DMT1, in the modulation of metal oxide uptake by OE cells. The DMT1 could either directly recognize divalent transition metal ions on the surface of NPs or interact with specific corona proteins, e.g., metalloproteins, bound to divalent transition metal NPs. Indeed, on the one hand, the interaction of some proteins with metal-oxide NP lattice has been shown [14], substantiating the possibility of direct recognition of divalent transition metals on the surface of NPs by the DMT1. On the other hand, even though NPs favor interactions with intrinsically disordered proteins, the exact composition of their protein corona depends on their exact chemical structure [18]. Thus, divalent transition metal NPs could bind to specific signature proteins recognized further by the DMT1 and/or other cell surface molecules [60]. These two possible mechanisms need further dissection to understand why divalent transition metal NPs are favored over other metal-oxide NPs in the olfactory neuronal uptake.

It has to be pointed out that compared to other studies [10, 11], here, we have investigated *in vivo* the olfactory neuronal uptake of unmodified metal oxide/hydroxide NPs. Thus, the conclusions regarding the specificity of neuronal uptake of unmodified vs. surface-modified inorganic NPs by ORNs vs. cultured neurons might differ. For example, surface-modified NPs lacking the divalent transition metal ions (Fe_2O_3, TiO_2, and SiO_2) could be readily engulfed by cultured neurons [9, 11].

For a detailed quantitative account of the spatiotemporal dynamics of NPs' N2B transmission, we have chosen the Mn_3O_4-NPs. The Mn_3O_4-NPs had high r_1 relaxivity in the MOB and, unlike soluble Mn^{2+} ions, had no impact on odor recognition, making them suitable as a probe for the *in vivo* T_1W MRI. We showed that the Mn_3O_4-NPs entered ORNs via cilia and largely remained in nanoparticulate form within the neurons. The axonal transport and trans-synaptic transmission of the Mn_3O_4-NPs depended on neuronal activity, aging, and the onset of the PD and could be modulated by odor stimuli.

In the absence of an odor, the Mn_3O_4-NP axonal transport seemed to require a spontaneous neuronal action potential and microtubule integrity, in line with other studies [9]. The NPs were translocated inside and outside vesicles with fast and slow axonal transport velocities. The trans-synaptic transmission of Mn_3O_4-NPs between ORNs and mitral/tufted cells was positively modulated by the activity of N-type Ca_v ($Ca_{v2.2}$) and NMDA-R and negatively by $GABA_B$-R. Consequently, our results provide new insights into the mechanism of the trans-synaptic transmission of NPs.

As such, a fraction of the Mn_3O_4-NPs was localized to the vesicles at synapses of ORN and hippocampal neurons (Fig. 2(a) and Fig. S4(e) in the ESM). Although further analysis requires to find out whether these are synaptic vesicles, it could be suggested that the mechanism of Mn_3O_4-NPs' release into the synaptic cleft is similar to that of neurotransmitters. Indeed, the presynaptic inhibition of ORN axon terminals by baclofen ($GABA_B$-R agonist) and cilnidipine ($Ca_v2.2$ blocker) hampers the synaptic vesicles exocytosis [61, 62] and, as a result, the trans-synaptic transmission of the Mn_3O_4-NPs (Figs. 3(c) and 3(d)). From the synaptic cleft, the NPs could enter adjacent neurons by either basal or regulated receptor-mediated postsynaptic endocytosis. NMDA, AMPA, and $GABA_A$ ionotropic receptors are located on the postsynaptic membrane [63, 64], and, thus, could modulate the trans-synaptic transmission of the Mn_3O_4-NPs. Interestingly, our results suggest that the activity of the NMDA receptor, but not of AMPA and $GABA_A$ receptors, is involved in the trans-synaptic transmission of

the Mn_3O_4-NPs (Figs. 3(c) and 3(d)). This selectivity could be potentially attributed to the presence of intrinsically disordered regions in the extracellular domains of GluN1, GluN2D, GluN3A, and GluN3B protein subunits of the NMDA receptor (Fig. S11 in the ESM). Previously we showed that NPs favor interactions with intrinsically disordered proteins [18], which could make the NMDA receptor a preferred target for the Mn_3O_4-NPs trans-synaptic transmission through the receptor-mediated postsynaptic endocytosis.

By T_1W MRI, we identified the principal N2B route for the Mn_3O_4-NP neuronal transmission (Fig. 4(b)). The transport of the Mn_3O_4-NPs from ORNs to the DG, LS, BST, SI, and IC depends on at least four trans-synaptic transmission events. The kinetic accumulation parameters of the Mn_3O_4-NPs for distinct brain structures across the olfactory tract negatively correlated with the putative numbers of synapses from ORNs (Figs. 4(d) and 4(e), and Fig. S8 and Tables S4 and S5 in the ESM). These data, in turn, substantiate our reconstruction of the N2B transport route. The $Pt(OH)_2$-NPs had similar N2B spatiotemporal dynamics (Fig. 1(b) and Fig. S2 in the ESM), indicating a common path for metal oxide/hydroxide NPs transportation across the olfactory tract.

The elimination rates of NPs from the brain were orders of magnitude slower than the accumulation and independent of a brain structure's position in the principal N2B route (Fig. 4(e), and Fig. S8 and Tables S4 and S5 in the ESM). Although the exact elimination mechanism is unclear, it may involve the slow dissolution of the NPs in the acidic environment of lysosomes (Fig. S5(h) in the ESM), exocytosis, or other mechanisms, such as mitosis [15, 65]. As the bulk of the Mn_3O_4-NPs was located outside of any vesicles (primarily in the cytosol and mitochondria of neurons) (Figs. 2(a) and 2(b)), this may explain their slow elimination kinetics. Exocytosis would require entrapment of the NPs inside secretory vesicles (lysosomes, exosomes, etc.). However, with a long enough time (days), NPs could be gradually packaged into secretory vesicles and expelled. Likewise, although mitosis is blocked in differentiated neurons, neurons that are not fully differentiated undergo cell divisions [66], which could also slowly reduce the load of NPs in neurons.

Consistent with the dependency of the NPs' axonal and synaptic translocation on neuronal activity, we found that relative accumulation rates of the Mn_3O_4-NPs inversely correlated with the number of synapses. Spontaneous neuronal activities are synchronized between ORNs and the areas receiving inputs from ORNs [44–46]. This observation implies that the Mn_3O_4-NPs are suitable for functional neuroimaging to trace spontaneous neuronal activity from an entry point across multiple synapses. Furthermore, we showed that the presentation of odor stimuli, such as 2,5DMP or acetophenone, led to the odor-evoked rerouting of the Mn_3O_4-NP N2B translocation path (Fig. 5). The new trajectories of neuronal transmission of Mn_3O_4-NPs were odor-dependent. Similar odor-induced modulation of the N2B transport route has been documented for Mn^{2+} [55]. However, intranasal administration of soluble Mn^{2+} ions, but not Mn_3O_4-NPs, interfered with odor recognition (Fig. S3(a) in the ESM), suggesting that the Mn_3O_4-NPs could be better suited for functional neuroimaging. To that, the ability of nanoparticles' N2B transport to be modulated by odor could create future opportunities for targeted drug delivery into specific brain structures. Although the surface of the Mn_3O_4-NPs is rather mundane, limiting its direct applications as a drug delivery system, in future studies, the Mn_3O_4-NPs could be capped with PEG or other surface-modifying molecules for drug loading.

Finally, we showed that the trans-synaptic transmission of Mn_3O_4-NPs from the GL to ML declined with aging, and it was further impaired in mice expressing the mutant alpha-Syn^{A53T} (Fig. 6). Moreover, deviation from the reference model dynamics of the GL-to-ML trans-synaptic transmission could discriminate with high-confidence individual male mice carrying the mutant alpha-Syn^{A53T} from wild-type starting from the age of 30 weeks. Aging and neurodegeneration cause olfactory dysfunction and reduction in spontaneous neuronal activity [68] and, thus, could impair the trans-synaptic transmission of the Mn_3O_4-NPs. As a result, the Mn_3O_4-NPs could be used to diagnose age-related neuronal decline and the onset of neurodegenerations, such as PD, without interfering with odor recognition and olfactory function (Fig. S3(a) in the ESM). However, although single intranasal administrations of the Mn_3O_4-NPs were seemingly safe to mice, chronic (many years) exposure to polluting NPs could cause a slight, but significant, increase in the risks of neurodegenerative diseases [2, 46]. Indeed, the NPs could provoke cellular stress and stress granules formation [15, 18], thus, acting as potential triggers of neurodegeneration [67]. In addition, the neurotoxicity of Mn^{2+} ions, which could be slowly released from the surface of the Mn_3O_4-NPs, could also impose a safety concern for the use of Mn_3O_4-NPs in diagnostics. However, the issues of the potential Mn_3O_4-NPs toxicity could be balanced through adequate dosing. To that, the Mn_3O_4-NPs have lower cytotoxicity and adverse effect on the olfactory recognition than $MnCl_2$ (Fig. S3 in the ESM), at the same time the $MnCl_2$ is already extensively used for the manganese-enhanced MRI in preclinical and even some pilot clinical studies [68].

4 Materials and methods

4.1 Synthesis and characterization of NPs

The Mn_3O_4, $MnFe_2O_4$, $CoFe_2O_4$, $MgFe_2O_4$, $Pt(OH)_2$, and $Ru(OH)_3$ were synthesized as previously described [15, 69]; see the Methods section in the ESM for details. Gd_2O_3, Mn_2O_3, and Fe_3O_4 were purchased from the US Research Nanomaterials, Inc. The d_h and ζ of the NPs were determined with Zetasizer Nano ZS (Malvern) at 90° according to the manufacturer's protocols. The relaxation time was estimated with BioSpec 117/16 USR (Bruker) at a magnetic field strength of 11.7 T by rapid acquisition with relaxation enhancement (RARE) (the Methods section in the ESM). The Mn_3O_4 NPs' morphology, interplanar distances, and chemical composition were studied by HRTEM under a JEM 2010 microscope equipped with a Super-X detector for EDXA (Jeol). Cellular uptake and localization of the Mn_3O_4 NPs in mouse hippocampal neurons were studied by TEM (the Methods section in the ESM).

4.2 Animal studies

Experiments on the NPs' neuronal uptake in the MOB and the N2B transport of Mn_3O_4-NPs and $Pt(OH)_2$-NPs were performed on specific pathogen-free (SPF) BALB/c male mice aged 12–14 weeks (the Methods section in the ESM). Comparisons of the Mn_3O_4-NPs' accumulation dynamics were performed for C57BL/6 and Hualpha-Syn(A53T) Parkinson's disease model strain on the C57BL/6 background [57] at the ages of 8, 30, and 38 weeks. A 7 μL of a colloidal solution containing 10 mg/mL of NPs was administered intranasally to awake mice in the prone position. In the supine position, NPs entered the stomach flowing through the nasal passage and omitting the olfactory epithelium.

4.3 Modulators of the Mn_3O_4-NPs' N2B transport

Metal chlorides at concentrations of 1 mM and other pharmaceuticals (Table S3(a) in the ESM) were injected into the nasal cavity 10 min before the Mn_3O_4-NP administration to investigate the mechanism of NPs' uptake in the OE. The T_1W MRI signal was evaluated in the OE one hour after the NPs administration. The inhibitors of axonal transport, action

potential, and synaptic activity were administered intranasally 1 h after the Mn_3O_4-NP administration at the final concentrations indicated in the main text and Table S3(b) in the ESM. The T_1W MRI signal was evaluated in the OE and MOB 24 h after the NP administration. All the inhibitors were diluted in 60 mM NaCl, 1 mM $CaCl_2$, and 10 mM KCl solution isosmotic to mucus [70] and injected in a volume of 7 μL in the same nostril as the NPs. The effects of each inhibitor were evaluated on eight animals.

For odor modulation of the Mn_3O_4-NPs' N2B transport, 0.01% solutions of 2,5DMP or PhAc were presented to BALB/c male mice. The animals were odor-stimulated 24 h after administering the Mn_3O_4-NPs in 10 sessions for 5 min with 55 min intervals using an olfactometer (Fig. S9 in the ESM). The animals were maintained on the 14 h:10 h light/dark cycle, and the odors were presented during the dark period at 200 mL/min.

4.4 TEM, HRTEM-EDXA, and ICP-AES analyses of the Mn_3O_4-NP neuronal uptake in mice

For TEM, the NPs were administered into the right nostril, and MOB samples from the right and left bulb were prepared and assayed separately 24 h after the administration of NPs. The MOB samples were fixed as described elsewhere [71], and ultrathin slices were prepared and examined under a JEM 100 SX transmission electron microscope (Jeol) (see the Methods section in the ESM for details). HRTEM-EDXA analysis was performed to assess interplanar distances and chemical composition of the NPs on the MOB slices using JEM 2010 equipped with a Super-X EDXA detector (Jeol). ICP-AES was carried out on an iCAP 6300 Duo instrument (Thermo Scientific) 24 h after Mn_3O_4-NP administration: (1) to measure a cellular vs. extracellular Mn content in the MOB; (2) to estimate a soluble vs. insoluble Mn content in the MOB neurons; (3) to determine the subcellular localization of the Mn_3O_4-NPs in the MOB neurons, and (4) to calibrate T_1W MRI signal intensities in the MOB to a series of Mn concentrations (see the Methods section in the ESM for details).

4.5 MRI of the Mn_3O_4-NP N2B transport

Accumulation of paramagnetic Mn_3O_4-NPs in mouse brain structures was studied at 11.7 T on a high-field MRI scanner, BioSpec 117/16 USR (Bruker), in combination with a mouse brain circular polarized MRI transceiver coil for 1H (Bruker BioSpin MRI). Five minutes before the analysis, mice were immobilized with 4% isoflurane using a Univentor 400 anesthesia unit (Univentor) and kept under 1.9% isoflurane anesthesia during the MRI scanning. T_1-weighted RARE images were captured with a pulse sequence of the time of echo (TE) of 10 ms and time of repetition (TR) of 400 ms. The total scan time was 6 min, and the imaging parameters were as follows: field of view 2.5 cm × 2.5 cm, matrix 512 × 512 points, slice thickness 0.5 mm, interslice distance 0.5 mm, and the number of slices: 15. MRI images were processed and quantified in the Image J software (the Methods section in the ESM). T_1W MRI signal intensities were first normalized to an external (phosphate buffer) signal present in each scan and then to a reference T_1W MRI signal measured for each animal before Mn_3O_4-NP administration. The resulting T_1W intensities were expressed as

$$S_{[Mn]} = \log_2(S_{T_1W}/S_{ref}) \quad (1)$$

where S_{T_1W} T_1W MRI signal is intensity after the administration and S_{ref} is that before the administration. The scans were obtained from six animals at 0.25, 0.5, 1, 2, 4, 12, 24, 48, 96, 168, 336, and 672 h after administration of 7 μL of 10 mg/mL Mn_3O_4-NPs into the right nostril.

4.6 Quantitative modeling of the Mn_3O_4-NP dynamics and statistical analysis

Statistical analyses of the data (linear and nonlinear regression models, *t*-test, and correlation analyses) were implemented in R. The Levenberg–Marquardt algorithm was used to fit the data to nonlinear regression models. T_1W MRI signal intensities for Mn_3O_4-NP accumulation/elimination dynamics were fitted to a five-parameter function

$$S_{[Mn]}(t) = S_a\left[1-\exp\left(-(t/\tau_{acc})^{\beta_{acc}}\right)\right]\exp\left(-(t/\tau_{dec})^{\beta_{dec}}\right) \quad (2)$$

consisting of the Weibull CDF

$$F_{acc}(t) = 1-\exp\left(-(t/\tau_{acc})^{\beta_{acc}}\right) \quad (3)$$

and its complement

$$F_{dec}(t) = \exp\left(-(t/\tau_{dec})^{\beta_{dec}}\right) \quad (4)$$

where S_a denotes the asymptotic maximum of $S_{[Mn]}(t)$; τ_{acc} and τ_{dec}—characteristic accumulation/decay times, respectively; and β_{acc} and β_{dec}—shape parameters. From this model, the rate function for Mn_3O_4-NP accumulation/elimination could be derived as

$$R_{[Mn]}(t) = \partial S_{[Mn]}(t)/\partial t \quad (5)$$

and other kinetic parameters could be estimated (the Methods section in the ESM). Although the Weibull accumulation/elimination curves were chosen empirically, the Weibull distribution effectively describes the wait time to one event.

Acknowledgements

This work was supported by a grant from the Russian Foundation for Basic Research RFBR (No. 20-16-00078). This work was conducted using the equipment the Centers of Collective Use "National Center of Catalyst Research" of Boreskov Institute of Catalysis SB RAS and by the budget project (No. FWNR-2022-0023 and project FWNR-2022-0004) and implemented using the equipment of the Center for Genetic Resources of Laboratory Animals at ICG SB RAS, supported by the Ministry of Education and Science of Russia (Unique identifier of the project RFMEFI62119X0023). TEM imaging was performed at the Microscopy Center of Biological Subjects ICG SB RAS (project #0259-2021-0011). The English language was corrected and certified by shevchuk-editing.com.

Electronic Supplementary Material: Supplementary material (Synthesis of nanoparticles. Relaxivity of the NPs. Cellular uptake and localization of the Mn_3O_4-NPs in hippocampal neurons. TEM analysis of Mn_3O_4-NP neuronal localization in the MOB. Animals. Olfactory threshold test and cytotoxicity. TEM analysis of Mn_3O_4 and $Pt(OH)_2$ NPs neuronal localization in the MOB. ICP-AES analysis of Mn_3O_4-NP neuronal localization in the MOB. MRI data processing. Micro-XRF analysis of the $Pt(OH)_2$-NPs and $Ru(OH)_3$-NPs brain localization. MRI data processing. Quantitative modeling of Mn_3O_4-NP accumulation/elimination dynamics. Figure S1. T_1W and T_2*W MRI of the NPs accumulation in the OE and MOB. Figure S2. Spatiotemporal N2B accumulation of the $Pt(OH)_2$-NPs. Figure S3. Olfactory threshold test and cytotoxicity of the Mn_3O_4-NPs. Figure S4. Synthesis and neuronal uptake of the Mn_3O_4-NPs. Figure S5. *In vivo* and *in vitro* solubility of the Mn_3O_4-NPs; HRTEM-EDXA

and ICP-AES of the Mn_3O_4-NPs in the MOB. Figure S6. Effects of the inhibitors of axonal transport and synaptic transmission on Mn_3O_4-NP accumulation in the MOB. Figure S7. Models of the Mn_3O_4-NP accumulation/elimination dynamics in the brain structures along the olfactory tract. Figure S8. Correlations of the Mn_3O_4-NP accumulation/elimination kinetic parameters with numbers of synaptic connections from the OE. Figure S9. Odor presentation. Figure S10. Effects of aging and alpha-Syn^{A53T} on accumulation dynamics of the Mn_3O_4-NPs in the MOB. Figure S11. Intrinsically disordered regions in the protein subunits of $GABA_A$, AMPA, and NMDA receptors. Table S1. The physicochemical properties of nanoparticles. Table S2. The r_1 relaxivity of the Mn_3O_4-NPs and $MnCl_2$ at a magnetic field strength of 11.7 T. Table S3(a). Modulators of the Mn_3O_4-NP neuronal uptake. Table S3(b). Modulators of the Mn_3O_4-NP axonal transport and trans-synaptic transmission. Table S4. Fitted coefficients of the Mn_3O_4-NP T_1W MRI signal accumulation/decay models. Table S5. The model-estimated dynamics of the Mn_3O_4-NP T_1W MRI signal accumulation/decay. Table S6. The model-estimated accumulation of the Mn_3O_4-NPs in C57BL/6 and PD mouse model strain Hualpha-Syn (A53T)) is available in the online version of this article at https://doi.org/10.1007/s12274-022-5302-6.

Abbreviations: AI: agranular insular area; AON: anterior olfactory nuclei; BST: bed nucleus of the stria terminalis; CA3: Cornu Ammonis area 3; CeA: central amygdaloid nucleus; CoA: cortical amygdala; DG: dentate gyrus; ENTl: lateral entorhinal cortex; ENTm: medial entorhinal cortex; EPL: external plexiform layer; GL: glomerular layer; GrL: granule cell layer; IC: inferior colliculus; LOT: lateral olfactory tract; MA: magnocellular nucleus; MEA: medial amygdalar nucleus; ML: mitral cell layer; MOB: main olfactory bulb; OE: olfactory epithelium; ORN: olfactory receptor neuron; OT: olfactory tubercles; PERI: perirhinal area; PIR: piriform cortex; SI: substantia innominata of the ventral pallidum; SNr: substantia nigra; SSp: primary somatosensory area; STN: subthalamic nucleus; VISp: primary visual area.

References

[1] Maher, B. A.; Ahmed, I. A. M.; Karloukovski, V.; MacLaren, D. A.; Foulds, P. G.; Allsop, D.; Mann, D. M. A.; Torres-Jardón, R.; Calderon-Garciduenas, L. Magnetite pollution nanoparticles in the human brain. *Proc. Natl. Acad. Sci. USA* **2016**, *113*, 10797–10801.

[2] Chen, H.; Kwong, J. C.; Copes, R.; Tu, K. R.; Villeneuve, P. J.; Van Donkelaar, A.; Hystad, P.; Martin, R. V.; Murray, B. J.; Jessiman, B. et al. Living near major roads and the incidence of dementia, Parkinson's disease, and multiple sclerosis: A population-based cohort study. *Lancet* **2017**, *389*, 718–726.

[3] Betzer, O.; Perets, N.; Angel, A.; Motiei, M.; Sadan, T.; Yadid, G.; Offen, D.; Popovtzer, R. *In vivo* neuroimaging of exosomes using gold nanoparticles. *ACS Nano* **2017**, *11*, 10883–10893.

[4] Khan, A. R.; Liu, M. R.; Khan, M. W.; Zhai, G. X. Progress in brain targeting drug delivery system by nasal route. *J. Control. Release* **2017**, *268*, 364–389.

[5] Pardo, M.; Roberts, E. R.; Pimentel, K.; Yildirim, Y. A.; Navarrete, B.; Wang, P.; Zhang, E.; Liang, P.; Khizroev, S. Size-dependent intranasal administration of magnetoelectric nanoparticles for targeted brain localization. *Nanomed. Nanotechnol. Biol. Med.* **2021**, *32*, 102337.

[6] Yokel, R. A. Nanoparticle brain delivery: A guide to verification methods. *Nanomedicine* **2020**, *15*, 409–432.

[7] Wang, Z. A.; Xiong, G. J.; Tsang, W. C.; Schätzlein, A. G.; Uchegbu, I. F. Nose-to-brain delivery. *J. Pharmacol. Exp. Ther.* **2019**, *370*, 593–601.

[8] Liu, Q. F.; Zhang, Q. Z. Nanoparticle systems for nose-to-brain delivery. In *Brain Targeted Drug Delivery System*; Gao, H. L.; Gao, X. L., Eds.; Elsevier: Amsterdam, 2019; pp 219–239.

[9] Kastrinaki, G.; Samsouris, C.; Kosmidis, E. K.; Papaioannou, E.; Konstandopoulos, A. G.; Theophilidis, G. Assessing the axonal translocation of CeO_2 and SiO_2 nanoparticles in the sciatic nerve fibers of the frog: An *ex vivo* electrophysiological study. *Int. J. Nanomed.* **2015**, *10*, 7089–7096.

[10] Walters, R.; Kraig, R. P.; Medintz, I.; Delehanty, J. B.; Stewart, M. H.; Susumu, K.; Huston, A. L.; Dawson, P. E.; Dawson, G. Nanoparticle targeting to neurons in a rat hippocampal slice culture model. *ASN Neuro* **2012**, *4*, 383–392.

[11] Dante, S.; Petrelli, A.; Petrini, E. M.; Marotta, R.; Maccione, A.; Alabastri, A.; Quarta, A.; De Donato, F.; Ravasenga, T.; Sathya, A. et al. Selective targeting of neurons with inorganic nanoparticles: Revealing the crucial role of nanoparticle surface charge. *ACS Nano* **2017**, *11*, 6630–6640.

[12] Lesniak, A.; Kilinc, D.; Blasiak, A.; Galea, G.; Simpson, J. C.; Lee, G. U. Rapid growth cone uptake and dynein-mediated axonal retrograde transport of negatively charged nanoparticles in neurons is dependent on size and cell type. *Small* **2019**, *15*, 1803758.

[13] Chen, L. P.; Li, X. J.; Zhang, Y. H.; Chen, T. W.; Xiao, S. Y.; Liang, H. J. Morphological and mechanical determinants of cellular uptake of deformable nanoparticles. *Nanoscale* **2018**, *10*, 11969–11979.

[14] Chao, Y.; Karmali, P. P.; Mukthavaram, R.; Kesari, S.; Kouznetsova, V. L.; Tsigelny, I. F.; Simberg, D. Direct recognition of superparamagnetic nanocrystals by macrophage scavenger receptor SR-AI. *ACS Nano* **2013**, *7*, 4289–4298.

[15] Illarionova, N. B.; Morozova, K. N.; Petrovskii, D. V.; Sharapova, M. B.; Romashchenko, A. V.; Troitskii, S. Y.; Kiseleva, E.; Moshkin, Y. M.; Moshkin, M. P. "Trojan-horse" stress-granule formation mediated by manganese oxide nanoparticles. *Nanotoxicology* **2020**, *14*, 1432–1444.

[16] Chen, Y.; Yin, Q.; Ji, X. F.; Zhang, S. J.; Chen, H. R.; Zheng, Y. Y.; Sun, Y.; Qu, H. Y.; Wang, Z.; Li, Y. P. et al. Manganese oxide-based multifunctionalized mesoporous silica nanoparticles for pH-responsive MRI, ultrasonography and circumvention of MDR in cancer cells. *Biomaterials* **2012**, *33*, 7126–7137.

[17] Amiri, H.; Bordonali, L.; Lascialfari, A.; Wan, S.; Monopoli, M. P.; Lynch, I.; Laurent, S.; Mahmoudi, M. Protein corona affects the relaxivity and MRI contrast efficiency of magnetic nanoparticles. *Nanoscale* **2013**, *5*, 8656–8665.

[18] Romashchenko, A. V.; Kan, T. W.; Petrovski, D. V.; Gerlinskaya, L. A.; Moshkin, M. P.; Moshkin, Y. M. Nanoparticles associate with intrinsically disordered RNA-binding proteins. *ACS Nano* **2017**, *11*, 1328–1339.

[19] Shepherd, G. M. *The Synaptic Organization of the Brain*; Oxford University Press: New York, 2004.

[20] Bowman, A. B.; Aschner, M. Considerations on manganese (Mn) treatments for *in vitro* studies. *Neurotoxicology* **2014**, *41*, 141–142.

[21] Dunn, L. L.; Suryo Rahmanto, Y.; Richardson, D. R. Iron uptake and metabolism in the new millennium. *Trends Cell Biol.* **2007**, *17*, 93–100.

[22] Biswas, K.; Das Sarma, J. Effect of microtubule disruption on neuronal spread and replication of demyelinating and nondemyelinating strains of mouse hepatitis virus *in vitro*. *J. Virol.* **2014**, *88*, 3043–3047.

[23] Smith, R. S.; Hammerschlag, R.; Snyder, R. E.; Chan, H.; Bobinski, J. Action of brefeldin A on amphibian neurons: Passage of newly synthesized proteins through the Golgi complex is not required for continued fast organelle transport in axons. *J. Neurochem.* **1994**, *62*, 1698–1706.

[24] Sheets, M. F.; Hanck, D. A. Outward stabilization of the S4 segments in domains III and IV enhances lidocaine block of sodium channels. *J. Physiol.* **2007**, *582*, 317–334.

[25] Stakic, J.; Suchanek, J. M.; Ziegler, G. P.; Griff, E. R. The source of spontaneous activity in the main olfactory bulb of the rat. *PLoS One* **2011**, *6*, e23990.

[26] Paxinos, G. *The Rat Nervous System*; 3rd ed. Academic Press: San Diego, 2004.

[27] Isaacson, J. S.; Vitten, H. $GABA_B$ receptors inhibit dendrodendritic transmission in the rat olfactory bulb. *J. Neurosci.* **2003**, *23*, 2032–2039.
[28] Uneyama, H.; Uchida, H.; Konda, T.; Yoshimoto, R.; Akaike, N. Selectivity of dihydropyridines for cardiac L-type and sympathetic N-type Ca^{2+} channels. *Eur. J. Pharmacol.* **1999**, *373*, 93–100.
[29] Weiss, J.; Pyrski, M.; Weissgerber, P.; Zufall, F. Altered synaptic transmission at olfactory and vomeronasal nerve terminals in mice lacking N-type calcium channel $Ca_v2.2$. *Eur. J Neurosci.* **2014**, *40*, 3422–3435.
[30] Panzanelli, P.; Perazzini, A. Z.; Fritschy, J. M.; Sassoè-Pognetto, M. Heterogeneity of γ-aminobutyric acid type A receptors in mitral and tufted cells of the rat main olfactory bulb. *J. Comp. Neurol.* **2005**, *484*, 121–131.
[31] Brown, N.; Kerby, J.; Bonnert, T. P.; Whiting, P. J.; Wafford, K. A. Pharmacological characterization of a novel cell line expressing human $\alpha_4\beta_3\delta$ $GABA_A$ receptors. *Br. J. Pharmacol.* **2002**, *136*, 965–974.
[32] Sassoé-Pognetto, M.; Utvik, J. K.; Camoletto, P.; Watanabe, M.; Stephenson, F. A.; Bredt, D. S.; Ottersen, O. P. Organization of postsynaptic density proteins and glutamate receptors in axodendritic and dendrodendritic synapses of the rat olfactory bulb. *J. Comp. Neurol.* **2003**, *463*, 237–248.
[33] Twomey, E. C.; Yelshanskaya, M. V.; Vassilevski, A. A.; Sobolevsky, A. I. Mechanisms of channel block in calcium-permeable AMPA receptors. *Neuron* **2018**, *99*, 956–968.e4.
[34] Murphy, G. J.; Glickfeld, L. L.; Balsen, Z.; Isaacson, J. S. Sensory neuron signaling to the brain: Properties of transmitter release from olfactory nerve terminals. *J. Neurosci.* **2004**, *24*, 3023–3030.
[35] Münster-Wandowski, A.; Gómez-Lira, G.; Gutiérrez, R. Mixed neurotransmission in the hippocampal mossy fibers. *Front. Cell. Neurosci.* **2013**, *7*, 210.
[36] Piatti, V. C.; Ewell, L. A.; Leutgeb, J. K. Neurogenesis in the dentate gyrus: Carrying the message or dictating the tone. *Front. Neurosci.* **2013**, *7*, 50.
[37] Wirtshafter, H. S.; Wilson, M. A. Lateral septum as a nexus for mood, motivation, and movement. *Neurosci. Biobehav. Rev.* **2021**, *126*, 544–559.
[38] David, A.; Pierre, L. Hippocampal neuroanatomy. In *The Hippocampus Book*. Andersen, P.; Morris, R.; Amaral, D.; Bliss, T.; O'Keefe, J., Eds.; Oxford University Press: New York, 2007; pp 37–114.
[39] Cádiz-Moretti, B.; Abellán-Álvaro, M.; Pardo-Bellver, C.; Martínez-García, F.; Lanuza, E. Afferent and efferent projections of the anterior cortical amygdaloid nucleus in the mouse. *J. Comp. Neurol.* **2017**, *525*, 2929–2954.
[40] Dong, H. W.; Petrovich, G. D.; Swanson, L. W. Topography of projections from amygdala to bed nuclei of the stria terminalis. *Brain Res. Rev.* **2001**, *38*, 192–246.
[41] Marsh, R. A.; Fuzessery, Z. M.; Grose, C. D.; Wenstrup, J. J. Projection to the inferior colliculus from the basal nucleus of the amygdala. *J. Neurosci.* **2002**, *22*, 10449–10460.
[42] Perge, J. A.; Niven, J. E.; Mugnaini, E.; Balasubramanian, V.; Sterling, P. Why do axons differ in caliber? *J. Neurosci.* **2012**, *32*, 626–638.
[43] Brown, A. Slow axonal transport: Stop and go traffic in the axon. *Nat. Rev. Mol. Cell Biol.* **2000**, *1*, 153–156.
[44] Lagier, S.; Carleton, A.; Lledo, P. M. Interplay between local GABAergic interneurons and relay neurons generates γ oscillations in the rat olfactory bulb. *J. Neurosci.* **2004**, *24*, 4382–4392.
[45] Poo, C.; Isaacson, J. S. Odor representations in olfactory cortex: "Sparse" coding, global inhibition, and oscillations. *Neuron* **2009**, *62*, 850–861.
[46] Fontanini, A.; Spano, P.; Bower, J. M. Ketamine-xylazine-induced slow (< 1.5 Hz) oscillations in the rat piriform (olfactory) cortex are functionally correlated with respiration. *J. Neurosci.* **2003**, *23*, 7993–8001.
[47] Kealy, J.; Commins, S. The rat perirhinal cortex: A review of anatomy, physiology, plasticity, and function. *Prog. Neurobiol.* **2011**, *93*, 522–548.
[48] Vismer, M. S.; Forcelli, P. A.; Skopin, M. D.; Gale, K.; Koubeissi, M. Z. The piriform, perirhinal, and entorhinal cortex in seizure generation. *Front. Neural Circuits* **2015**, *9*, 27.
[49] Schneider, N. Y.; Chaudy, S.; Epstein, A. L.; Viollet, C.; Bénani, A.; Pénicaud, L.; Grosmaître, X.; Datiche, F.; Gascuel, J. Centrifugal projections to the main olfactory bulb revealed by transsynaptic retrograde tracing in mice. *J. Comp. Neurol.* **2020**, *528*, 1805–1819.
[50] Saper, C. B. Organization of cerebral cortical afferent systems in the rat. II. Magnocellular basal nucleus. *J. Comp. Neurol.* **1984**, *222*, 313–342.
[51] Krusemark, E. A.; Novak, L. R.; Gitelman, D. R.; Li, W. When the sense of smell meets emotion: Anxiety-state-dependent olfactory processing and neural circuitry adaptation. *J. Neurosci.* **2013**, *33*, 15324–15332.
[52] Shi, C. J.; Cassell, M. Cortical, thalamic, and amygdaloid connections of the anterior and posterior insular cortices. *J. Comp. Neurol.* **1998**, *399*, 440–468.
[53] Lee, H. J.; Gallagher, M.; Holland, P. C. The central amygdala projection to the substantia nigra reflects prediction error information in appetitive conditioning. *Learn. Mem.* **2010**, *17*, 531–538.
[54] Zhou, M.; Liu, Z. H.; Melin, M. D.; Ng, Y. H.; Xu, W.; Südhof, T. C. A central amygdala to zona incerta projection is required for acquisition and remote recall of conditioned fear memory. *Nat. Neurosci.* **2018**, *21*, 1515–1519.
[55] Fa, Z. Q.; Zhang, P.; Huang, F. H.; Li, P.; Zhang, R.; Xu, R. X.; Wen, Z. B.; Jiang, X. D. Activity-induced manganese-dependent functional MRI of the rat visual cortex following intranasal manganese chloride administration. *Neurosci. Lett.* **2010**, *481*, 110–114.
[56] Kondo, K.; Kikuta, S.; Ueha, R.; Suzukawa, K.; Yamasoba, T. Age-related olfactory dysfunction: Epidemiology, pathophysiology, and clinical management. *Front. Aging Neurosci.* **2020**, *12*, 208.
[57] Lee, M. K.; Stirling, W.; Xu, Y. Q.; Xu, X. Y.; Qui, D.; Mandir, A. S.; Dawson, T. M.; Copeland, N. G.; Jenkins, N. A.; Price, D. L. Human α-synuclein-harboring familial Parkinson's disease-linked Ala-53 → Thr mutation causes neurodegenerative disease with α-synuclein aggregation in transgenic mice. *Proc. Natl. Acad. Sci. USA* **2002**, *99*, 8968–8973.
[58] Zhang, S. F.; Xiao, Q.; Le, W. D. Olfactory dysfunction and neurotransmitter disturbance in olfactory bulb of transgenic mice expressing human A53T mutant α-synuclein. *PLoS One* **2015**, *10*, e0119928.
[59] Mistry, A.; Stolnik, S.; Illum, L. Nose-to-brain delivery: Investigation of the transport of nanoparticles with different surface characteristics and sizes in excised porcine olfactory epithelium. *Mol. Pharmaceutics* **2015**, *12*, 2755–2766.
[60] Aliyandi, A.; Zuhorn, I. S.; Salvati, A. Disentangling biomolecular corona interactions with cell receptors and implications for targeting of nanomedicines. *Front. Bioeng. Biotechnol.* **2020**, *8*, 599454.
[61] Isaacson, J. S.; Hille, B. $GABA_B$-mediated presynaptic inhibition of excitatory transmission and synaptic vesicle dynamics in cultured hippocampal neurons. *Neuron* **1997**, *18*, 143–152.
[62] Mochida, S. Neurotransmitter release site replenishment and presynaptic plasticity. *Int. J. Mol. Sci.* **2020**, *22*, 327.
[63] Attwell, D.; Gibb, A. Neuroenergetics and the kinetic design of excitatory synapses. *Nat. Rev. Neurosci.* **2005**, *6*, 841–849.
[64] Shrivastava, A. N.; Triller, A.; Sieghart, W. $GABA_A$ receptors:Post-synaptic co-localization and cross-talk with other receptors. *Front. Cell. Neurosci.* **2011**, *5*, 7.
[65] Bourquin, J.; Septiadi, D.; Vanhecke, D.; Balog, S.; Steinmetz, L.; Spuch-Calvar, M.; Taladriz-Blanco, P.; Petri-Fink, A.; Rothen-Rutishauser, B. Reduction of nanoparticle load in cells by mitosis but not exocytosis. *ACS Nano* **2019**, *13*, 7759–7770.
[66] Walton, C. C.; Zhang, W.; Patiño-Parrado, I.; Barrio-Alonso, E.;

Garrido, J. J.; Frade, J. M. Primary neurons can enter M-phase. *Sci. Rep.* **2019**, *9*, 4594.
[67] Fontanini, A.; Spano, P.; Bower, J. M. Ketamine-xylazine-induced slow (< 1.5 Hz) oscillations in the rat piriform (olfactory) cortex are functionally correlated with respiration. *J. Neurosci.* **2003**, *23*, 7993–8001.
[68] Kondo, K.; Kikuta, S.; Ueha, R.; Suzukawa, K.; Yamasoba, T. Age-related olfactory dysfunction: Epidemiology, pathophysiology, and clinical management. *Front. Aging Neurosci.* **2020**, *12*, 208.
[69] Yang, L. X.; Li, S.; Zhang, J.; Chen, Z.; Xu, S. C. Preparation, characterization and magnetic property of MFe_2O_4 (M= Mn, Zn, Ni, Co) nanoparticles. *Advanced Materials Research* **2014**, *842*, 35–38.
[70] Kozlova, I.; Vanthanouvong, V.; Marie, J.; Roomans, G. M. Composition of airway surface liquid determined by X-ray microanalysis. *Ups J Med Sci.* **2006**, *111*, 137–153.
[71] Stefanova, N. A.; Maksimova, K. Y.; Kiseleva, E.; Rudnitskaya, E. A.; Muraleva, N. A.; Kolosova, N. G. Melatonin attenuates impairments of structural hippocampal neuroplasticity in OXYS rats during active progression of Alzheimer's disease-like pathology. *Journal of Pineal Research* **2015**, *59*, 163–177.